The rocky road to quiescence: compaction and quenching of quasar host galaxies at z ~ 2

Stacey, H.R.; McKean, J.P.; Powell, D.M.; Vegetti, S.; Rizzo, F.; Spingola, C.; ... ; Werf, P.P. van der

The rocky road to quiescence: compaction and quenching of quasar host galaxies at z ~ 2

H. R. Stacey,[1,2,3]★ J. P. McKean,[1,2] D. M. Powell,[3] S. Vegetti,[3] F. Rizzo,[3] C. Spingola,[4,5]
M. W. Auger,[6,7] R. J. Ivison[8] and P. P. van der Werf[9]

[1]*ASTRON, Netherlands Institute for Radio Astronomy, Oude Hoogeveensedijk 4, 7991 PD, Dwingeloo, The Netherlands*
[2]*Kapteyn Astronomical Institute, University of Groningen, PO Box 800, 9700 AV Groningen, The Netherlands*
[3]*Max Planck Institute for Astrophysics, Karl-Schwarzschild Str. 1, D-85748 Garching bei München, Germany*
[4]*INAF − Istituto di Radioastronomia, Via Gobetti 101, I−40129, Bologna, Italy*
[5]*Dipartimento di Fisica e Astronomia, Università degli Studi di Bologna, Via Gobetti 93/2, I−40129 Bologna, Italy*
[6]*Institute of Astronomy, University of Cambridge, Madingley Road, Cambridge CB3 0HA, UK*
[7]*Kavli Institute for Cosmology, University of Cambridge, Madingley Road, Cambridge CB3 0HA, UK*
[8]*European Southern Observatory, Karl-Schwarzschild-Str. 2, D-85748 Garching bei München, Germany*
[9]*Leiden Observatory, Leiden University, PO Box 9513, NL-2300 RA Leiden, The Netherlands*

ABSTRACT

We resolve the host galaxies of seven gravitationally lensed quasars at redshift 1.5 to 2.8 using observations with the Atacama Large (sub-)Millimetre Array. Using a visibility-plane lens modelling technique, we create pixellated reconstructions of the dust morphology, and CO line morphology and kinematics. We find that the quasar hosts in our sample can be distinguished into two types: 1) galaxies characterised by clumpy, extended dust distributions ($R_{\rm eff} \sim 2$ kpc) and mean star formation rate surface densities comparable to sub-mm-selected dusty star-forming galaxies ($\Sigma_{\rm SFR} \sim 5$ $M_\odot$ yr^{-1} kpc^{-2}); 2) galaxies that have sizes in dust emission similar to coeval passive galaxies and compact starbursts ($R_{\rm eff} \sim 0.5$ kpc), with high mean star formation rate surface densities ($\Sigma_{\rm SFR} = 40$–2200 $M_\odot$ yr^{-1} kpc^{-2}) and peak densities of 280–3700 $M_\odot$ yr^{-1} kpc^{-2} that in some cases are Eddington-limited. The small sizes of some quasar hosts suggests that we observe them at a stage in their transformation into compact spheroids, where a high density of dynamically unstable gas leads to efficient star formation and black hole accretion. For the one system where we probe the mass of the gas reservoir, we find a gas fraction of just 0.06±0.04 and a depletion timescale of 50±40 Myr, suggesting it is transitioning into quiescence. In general, we expect that the extreme level of star formation in the compact quasar host galaxies will rapidly exhaust their gas reservoirs and could quench with or without help from active galactic nuclei feedback.

Key words: quasars: general – galaxies: evolution – galaxies: star formation – galaxies: high-redshift – submillimetre: galaxies – gravitational lensing: strong

1 INTRODUCTION

In the last two decades, large-area sub-millimetre surveys have revealed a population of high-redshift galaxies with extreme levels of star formation, which were largely undetected in optical surveys as their ultraviolet (UV) emission is obscured by dust (Blain et al. 2002; Casey et al. 2014, Hodge & da Cunha 2020 for reviews). These dusty star-forming galaxies (DSFGs) are expected to be precursors to locally observed massive elliptical galaxies, which are characterised by dense, old stellar populations with dispersion-dominated dynamics (Hopkins et al. 2008). A key aspect of the study of galaxy evolution is understanding how these galaxies formed such high stellar densities and grew concurrently with their central supermassive black holes (Magorrian et al. 1998). Recent near-infrared surveys have revealed that the population of compact quiescent galaxies start to appear at $z \sim 2$ and rapidly increase in number density before apparently declining at $z \sim 1$ (Trujillo et al. 2006; van Dokkum et al. 2008, 2015). These galaxies are around four times smaller in size than $z \sim 0$ massive ellipticals and are thought to form the centre of these galaxies, which later grow in size (but little in mass) due to a series of gas-poor, minor mergers (Naab et al. 2007, 2009).

The characteristics and rapid formation of compact quiescent galaxies can be reproduced if a very high density of gas is con-

★ E-mail: stacey@mpa-garching.mpg.de

centrated within a region of ~ 1 kpc to generate a brief, intense starburst (Valentino et al. 2020). However, the mechanisms that cause such rapid morphological change and quenching of star formation are currently unclear. Compaction may be due to a net loss of angular momentum that results from dynamical instabilities induced by gas-rich mergers or tidal interactions (Mihos & Hernquist 1996; Hopkins et al. 2008), or by non-axisymmetric structures caused by rapid accretion and clumpy star formation (Dekel et al. 2009; Zolotov et al. 2015). Alternatively, these galaxies could have formed secularly, in-situ at earlier epochs without the need for mergers or rapid evolution (Damjanov et al. 2011; Carollo et al. 2013; Williams et al. 2014; Wellons et al. 2015).

Star formation terminates as a result of depletion or cessation of the supply of molecular gas. In compact quiescent galaxies, this may happen as a result of compaction, where star formation is self-quenched by radiation pressure from massive stars and supernovae-driven winds (Murray et al. 2005; Andrews & Thompson 2011; Diamond-Stanic et al. 2012). Eddington-limited 'maximum' starbursts have been discovered in DSFGs at high redshift (Riechers et al. 2013; Oteo et al. 2016; Cañameras et al. 2017; Spilker et al. 2019) as well as in nearby ultra-luminous infrared galaxies (ULIRGs; Barcos-Muñoz et al. 2017). These can be sufficiently vigorous to drive large-scale outflows and quench their hosts (Cañameras et al. 2017; Spilker et al. 2018), from the inside-out, on timescales of 10s Myr (Spilker et al. 2019).

Hydro-dynamical simulations and semi-analytic models of galaxy formation find that feedback from active galactic nuclei (AGN) is necessary, in addition to stellar feedback, to reproduce observed galaxy stellar populations and luminosity functions (Di Matteo et al. 2005; Sijacki et al. 2007; Somerville et al. 2008; Schaye et al. 2015). AGN feedback occurs in the form of jets or radiative winds, which can suppress star formation by mechanically coupling to the molecular gas and/or by preventing (re-)accretion from the circumgalactic medium (Fabian 2012, for review).

Due to computational limitations, current cosmological simulations involve only phenomenological implementations of feedback, which are calibrated to match observational data (see Somerville & Davé 2015). Observations find circumstantial evidence that AGN could play a role in the evolution of their hosts, in that the compaction phase seems to coincide with the appearance of an AGN (Barro et al. 2013; Kocevski et al. 2017). However, studies have found conflicting results as to whether AGN have any effect on their host galaxies. While some earlier studies found evidence of suppressed star formation in AGN hosts (e.g. Page et al. 2012), more recent studies of statistical samples have found no correlation between star formation and black hole accretion (Harrison et al. 2012; Rosario et al. 2013; Harris et al. 2016; Stanley et al. 2017; Pitchford et al. 2016; Kirkpatrick et al. 2019; Schulze et al. 2019). This could be because the effects of AGN feedback can only be detected later, or because black hole accretion is stochastic (Gabor & Bournaud 2014; Hickox et al. 2014). Even in simulations, star-formation rates averaged over ~ 100 Myr can show no clear correlation with black hole accretion (Harrison 2017), suggesting the effect of AGN may not be obvious in studies of the global properties of quasar hosts.

These key tests of the evolutionary sequence require investigations of the size, structure and dynamical properties of individual quasar hosts during the cosmic peak of galaxy growth ($z \sim 2$). This demands high spatial resolution (100s pc), which is most efficiently achieved by observing objects that are gravitationally lensed (e.g. Swinbank et al. 2010; ALMA Partnership et al. 2015). By observing galaxies that are strongly gravitationally lensed, it is possible to recover the properties of the source with greater angular resolution and sensitivity. Stacey et al. (2018) conducted a survey of gravitationally lensed quasar systems with the *Herschel Space Observatory* to measure the level of obscured star formation in the quasar host galaxies. This paper presents observations with the Atacama Large (sub-)Millimetre Array (ALMA) of a sub-sample of seven optically luminous quasars from the parent sample of Stacey et al. to resolve their host galaxy emission. Using a pixellated lens modelling technique applied to the interferometric data, we reconstruct dust and gas in the host galaxies and derive their intrinsic properties. In Section 2 we describe the targets, observations and data reduction process. In Section 3 we describe our lens modelling and source reconstruction technique. Section 4 reports the results of the structure of dust and gas, gas dynamics and star formation properties of the individual objects. We compare the morphological and star formation properties of the quasar host galaxies with a sample of DSFGs. In Section 5, we discuss the implications of our results in the context of evolutionary models and possible avenues to test our conjectures. Section 6 presents a summary of our findings and avenues for future work.

Throughout, we assume the Planck Collaboration et al. (2016) instance of a flat ΛCDM cosmology with $H_0 = 67.8$ km s^{-1} Mpc^{-1}, $\Omega_M = 0.31$ and $\Omega_\Lambda = 0.69$.

2 SAMPLE AND OBSERVATIONS

In this section, we first summarise the sample, the observations with ALMA and the data reduction processes, before giving a detailed description of the properties of each target studied here.

2.1 Summary of the sample, observations and data reduction

The targets in this work are seven four-image gravitationally lensed quasar (Type 1 AGN) systems. Four targets, SDSS J0924+0219, PG 1115+080, WFI J2033−4723 and WFI J2026−4536 are from our own programme (PI: McKean) and were not selected on the basis of their FIR/sub-mm properties, but for the configuration of their lensed quasar images in optical data for reasons that are not relevant to this work. We also include here archival data of HS 0810+2554 (PI: Chartas), RX J0911+0551 (PI: Leung) and H1413+117 (PI: van der Werf), which are known to have bright sub-mm emission (Barvainis & Ivison 2002). Details of the observations are given in Table 1. From previous modelling of their spectral energy distributions (SEDs; Stacey et al. 2018; see Figs. 1 and 2) we expect the sub-mm emission to be entirely dominated by thermal dust. As these latter systems were primarily selected in optical imaging and subsequently selected on the basis of their FIR luminosity, their selection is largely insensitive to dust temperature. We compile all accessible data with sufficiently high angular resolution to resolve the size and structure of the emission from cold dust at sub-mm/mm wavelengths. As a result, this sample is heterogeneous, and the observations probe different CO line transitions (see Table 2).

The raw data were calibrated using the ALMA pipeline in the Common Astronomy Software Applications package (CASA; McMullin et al. 2007) to produce calibrated visibilities. The data were inspected to confirm the quality of the pipeline calibration and determine whether further flagging was required. RX J0911+0551, PG 1115+080, H1413+117 and WFI J2026−4536 were self-calibrated using the line-free spectral windows with solution intervals of each scan length. Self-calibration was attempted

Table 1. Summary of the targets and ALMA observations. We give the phase centre right ascension and declination (in degrees, J2000), lens and source redshift (from optical spectroscopy – improved redshift estimates for these systems are presented in Table 2), central frequency of the observation, total on-source integration, the FWHM of the naturally weighted beam, and project code for the seven targets in this work. The redshift of the lens is not known for HS 0810+2554, H1413+117 or WFI J2026−4536, but this has no bearing on our results.

	RA (deg)	Dec (deg)	z_l	z_s	ν_{obs} (GHz)	t_s (min)	FWHM (arcsec)	Project code
HS 0810+2254	123.38053	+25.75068	–	1.51	145 GHz	32	0.17×0.13	2017.1.01368.S
RX J0911+0551	137.86458	+05.84833	0.70	2.79	145 GHz	123	0.40×0.35	2017.1.01081.S
SDSS J0924+0219	141.23258	+02.32347	0.39	1.52	358 GHz	44	0.28×0.23	2018.1.01591.S
PG 1115+080	169.57083	+07.76603	0.31	1.74	346 GHz	27	0.32×0.21	2018.1.01591.S
H1413+117	213.94271	+11.49539	–	2.56	285 GHz	10	0.24×0.21	2012.1.00175.S
WFI J2026−4536	306.54346	−45.60753	–	2.22	350 GHz	28	0.14×0.14	2018.1.01591.S
WFI J2033−4723	308.42533	−47.39528	0.66	1.66	341 GHz	28	0.31×0.28	2018.1.01591.S

for SDSS J0924+0219 and WFI J2033−4723, but was not successful, probably because of the lower signal-to-noise ratio of the surface brightness. We did not attempt to self-calibrate the data for HS 0810+2554 as the continuum emission is extremely weak (see below).

The targets were imaged with natural weighting of the visibilities and deconvolved using CLEAN (Högbom 1974). The deconvolved images are shown in Figs. 2 to 8. The continuum emission is consistent with the level of thermal dust emission expected from SED-fitting (Stacey et al. 2018). We detect the host galaxies of the quasars that, in some cases, forms Einstein rings and gravitational arcs. We also find compact dust emission that, in all cases, approximately coincides with the quasar positions seen in optical data. No emission is detected from any of the lensing galaxies.

All data sets, except in the case of PG 1115+080, included observations of an emission line of CO. The spectral line data were prepared by fitting a linear model for the continuum to the line-free spectral windows and subtracting this from the visibilities. This produced a visibility data set that included only the line emission. The resulting line profiles, fit with single Gaussians, are shown in Fig. 1. In some cases, the line peaks are offset from the systemic velocity (the rest-frame of the galaxy), which is possibly due to an uncertainty in the inferred redshift from optical spectroscopy: redshifts of quasars determined from optical spectroscopy can trace outflows of ionised gas, leading to incorrect inference on the systemic velocity. A summary of the spectral line observations is presented in Table 2.

The spectral line moment maps (velocity-integrated flux density, velocity field, velocity dispersion) are shown in Figs. 2 to 7. The velocity field and velocity dispersion are made by masking channel pixels below a signal-to-noise ratio threshold (stated within the figure captions).

2.2 HS 0810+2554

HS 0810+2554 is a quasar at $z_s = 1.51$ that is lensed into a characteristic fold-configuration (Reimers et al. 2002; Hewett & Wild 2010). The redshift of the foreground galaxy is unknown, but is estimated to be 0.9 based on the lens population distribution (Mosquera & Kochanek 2011). This quasar is faint at radio wavelengths, but VLBI investigations find evidence of compact, low-luminosity radio-jet structure that dominates the radio emission (Hartley et al. 2019). HS 0810+2554 was observed with ALMA at 145 GHz, which also targeted the CO (3–2) emission line.

We resolve thermal dust emission from this system with ALMA at 145 GHz that has a peak surface brightness of 6σ (where

σ is the rms noise per beam). The achieved rms noise level is 13 μJy beam^{-1} with natural weighting. Emission is detected around the close images, where the magnification is high and there is a hint of emission from the counter images. The total flux density of 0.3 mJy is consistent with the level of thermal dust emission expected at the observing frequency, based on SED fitting (see Fig. 1). The weak synchrotron emission seen at cm wavelengths is not expected to be detectable at the higher frequencies investigated here.

The CO (3–2) line profile for HS 0810+2554 is shown in Fig. 1, which has a FWHM of about 380 ± 10 km s^{-1} based on a single Gaussian fit. We find that the peak of the line emission is shifted -465 ± 6 km s^{-1} from the assumed optical systemic velocity, likely due to an uncertain redshift estimate. ALMA imaging of the line emission shows that the molecular gas is extended and lensed into an Einstein ring (see Fig. 2).

2.3 RX J0911+0551

RX J0911+0551 (RX J0911.4+0551) is a quasar at $z_s = 2.79$ that is lensed by a foreground galaxy at $z_l = 0.77$ (Burud et al. 1998; Kneib et al. 2000). The lens system has a characteristic cusp configuration with three close images. The environment of this lens system is quite complex: the primary lens has a satellite galaxy within the Einstein radius, and the lens galaxy is part of a cluster that contributes a high level of tidal shear (Kneib et al. 2000). Investigations at radio wavelengths have not been able to determine whether there is radio jet emission (Jackson et al. 2015). However, its radio luminosity is consistent with the expectations for star formation based on the radio–infrared correlation (Stacey et al. 2018). For our analysis, we use ALMA imaging at 145 GHz that also targeted the CO (5–4) emission line from RX J0911+0551.

We detect thermal dust continuum for this system with a total flux density at 145 GHz of 1.4 mJy, consistent with the expectations from SED fitting (see Figs. 1 and 2). We achieve an rms noise of 7 μJy beam^{-1} with natural weighting of the visibilties. Imaging of the dust shows compact emission that is resolved around the triplet images (see Fig. 3). From the lens configuration, it is clear that the galaxy is crossing the cusp of the lens caustic.

The CO (5–4) line profile for RX J0911+0551 is presented in Fig. 1. The spatially integrated line profile has a FWHM of 133 ± 3 km s^{-1} based on a single Gaussian fit, which is similar to the 120 ± 14 km s^{-1} reported for the CO (7–6) line by Tuan-Anh et al. (2017). Imaging of the CO (5–4) line emission shows compact structure that is similar to the dust continuum (see Fig. 3). The imaging is visually similar to the CO (11–10), CO (10–9), CO (7–6) and CO (1–0) emission reported by Tuan-Anh et al. (2017) and

Sharon et al. (2016): none of which are extended into rings or arcs, suggesting the emission is similarly compact.

2.4   SDSS J0924+0219

SDSS J0924+0219 is a radio-quiet quasar at $z_s = 1.525$ that is lensed by a galaxy at $z_l = 0.39$ (Inada et al. 2003; Hewett & Wild 2010). This lens system was discovered at optical wavelengths and has a characteristic fold-configuration. Observations with ALMA at 358 GHz, which also targeted the CO (8–7) line, were taken as part of our own observing programme.

The continuum emission from SDSS J0924+0219 is detected with a total flux density of 9.5 mJy at 358 GHz, consistent with the expectations for thermal dust emission from SED fitting (see Fig. 1). We achieve an rms noise of 28 μJy beam^{-1} with natural weighting of the visibilities. The continuum imaging shows an Einstein ring of clumpy dust with compact emission at the locations of the quasar images. The extent of the dust seems consistent with a 'red' ring seen in optical/infrared imaging (Eigenbrod et al. 2006). The same study also finds lensed arcs from a 'blue' component, of which there is a suggestion in the ALMA imaging where the Southern arc appears to split. These different optical components could be evidence of an ongoing merger or interaction (e.g. Rybak et al. 2015b).

The CO (8–7) line profile is presented in Fig. 1. The line profile is found from a Gaussian fit to have a FWHM of 176 ± 11 km s^{-1} that is shifted by 36 ± 5 km s^{-1} from the optical systemic velocity. Imaging of the CO (see Fig. 4) shows resolved emission at the position of the quasar images and evidence for a velocity gradient in the two close images. The velocity gradient is similar to that reported by Badole et al. (2020) for CO (5–4), where the CO emission is more extended. The line profile has a similar FWHM, but the shape of the CO (8–7) is more peaked than for the CO (5–4) and the surface brightness sensitivity is lower.

2.5   PG 1115+080

PG 1115+080 is a quasar at $z_s = 1.74$ that is lensed by a galaxy at $z_l = 0.31$ (Weymann et al. 1980; Hewett & Wild 2010). Investigations at radio wavelengths have not been able to determine whether the quasar has radio jet emission (Jackson et al. 2015), however its radio luminosity is consistent with the expectations for star formation based on the radio–infrared correlation (Stacey et al. 2018). PG 1115+080 was targeted as part of our own programme with ALMA at 346 GHz.

We detect continuum emission with a total flux density of 2.6 mJy, consistent with the expectations for thermal dust emission from SED fitting (see Fig. 1). The imaging of the dust emission for PG 1115+080 is presented in Fig. 8 and shows compact structure at the position of the quasar images, without any evidence of an extended Einstein ring. Given that the total flux density is close to what is expected from this system, we do not believe that significant emission from an extended component has been resolved out with these data. However, the emission is marginally radially resolved around the two close images. Unlike in the cases of the other quasar hosts in this sample, the unobscured star formation seen in the optical and near-infrared appears more extended than in the obscured star formation we observe here (Sluse et al. 2012; Chen et al. 2019).

2.6   H1413+117

H1413+117 (the Cloverleaf) is a quasar at $z_s = 2.56$ that is lensed by a galaxy at unknown redshift (Magain et al. 1988; Riechers et al. 2011b). Due to its extreme luminosity at far-infrared (FIR) wavelengths, the lens system is one of the best studied quasar-starbursts. While it is not extremely radio-luminous, this system does have a radio-excess relative to its infrared luminosity (Stacey et al. 2018) and has evidence of structure at radio wavelengths that may be from a low-luminosity radio jet (Stacey et al. in prep). We use for our analysis archival data for H1413+117 that was taken at 285 GHz with ALMA, which also targeted the CO (9–8) emission line.

Thermal dust emission is detected in the ALMA imaging with a total flux density of 26 mJy and an rms noise level of 93 μJy beam^{-1}, using a natural weighting of the visibilities. The CO (9–8) line emission is detected with a spatially integrated peak flux density of 83 mJy and a FWHM of 394 ± 8 km s^{-1}, from a Gaussian profile fit (see Fig. 1); this is the brightest line emission detected from our sample.

We resolve the four images of the quasar host galaxy in continuum and the CO (9–8) molecular line emission, with high surface brightness peaks at the position of the quasar images and an extended, almost complete Einstein ring that connects them (see Fig. 5). The structure of the emission appears similar to previous observations of dust and gas in this system (Alloin et al. 1997; Ferkinhoff et al. 2015). We also identify an additional source with a flux density of $\simeq$ 3.5 mJy within the field at a distance $\sim$ 6 arcsec North of the lens. This is a potential source of confusion for the SED fitting, where the photometric measurements are typically made at a low angular resolution (e.g. IRAS or *Herschel*/SPIRE). This additional source may also explain the scatter in the photometric measurements from H1413+117 (e.g. see Stacey et al. 2018; Fig. 2). From a cursory inspection of the available ALMA archival data at a frequency of $\sim$ 100 GHz (project code 2015.1.01309.S), we find that the additional source is detected with a similar flux density ratio as at 290 GHz with respect to H1413+117, suggesting that these galaxies have similar redshifts.

2.7   WFI J2026−4536

WFI J2026−4536 is a quasar at $z = 2.22$ (Morgan et al. 2004) that is lensed by a galaxy at unknown redshift into four images in a typical fold configuration. There are no radio observations of this system available to characterise its radio properties at 1.4 GHz, but the lack of detection in the Sydney University Molonglo Sky Survey (SUMSS) Source Catalog (Mauch et al. 2003) suggests a radio flux density of < 12 mJy at 1.4 GHz, assuming a typical synchrotron spectral index of −0.7. WFI J2026−4536 was observed with ALMA at 350 GHz as part of our ALMA programme, which also observed the CO (10–9) spectral line transition.

The ALMA observations detect continuum emission with a flux density of 28.3 mJy and achieve an rms noise level of 30 μJy beam^{-1} with natural weighting. This flux density is in good agreement with thermal dust emission, based on SED fitting (Fig. 2). The CLEANed image shows bright emission from the location of the quasar images and extended emission at lower surface brightness.

The CO (10–9) line emission is also spatially resolved with a similar morphology to the dust emission. The spatially integrated CO line profile has a peak flux density of 49 mJy and shows a hint of a double-horned feature characteristic of disc kinematics. The

FWHM of the line is 252±7 km s^{-1} and is offset by ∼ 1000 km s^{-1} from the systemic velocity assumed from optical spectroscopy.

2.8 WFI J2033−4723

WFI J2033−4723 is a quasar at $z_s = 1.66$ that is lensed by a galaxy at $z_l = 0.66$ (Morgan et al. 2004) into four images in a typical fold configuration. The lack of detection in the SUMSS suggests a radio flux density of < 12 mJy at 1.4 GHz. No other radio observations are available for this lens system. The target was observed with ALMA at 341 GHz as part of our programme, which also observed the CO (8–7) emission line from the lensed quasar.

The ALMA observations detect thermal dust emission with a total flux density of 10.4 mJy and achieve an rms noise of 30 μJy beam^{-1} with natural weighting of the visibilities. Imaging of WFI J2033−4723 shows a ring of extended, clumpy dust emission and compact emission from the approximate location of the quasar images (see Fig. 7). Arcs of faint emission from the host galaxy have also been observed at optical wavelengths, similar to the extended dust emission observed here (Rusu et al. 2020). The observed flux-density at 341 GHz is in good agreement with the expectations of SED fitting to a thermal dust model (see Fig. 2).

We detect the CO (8–7) line emission with a spatially integrated peak flux density of 11 mJy. The FWHM of the line profile is quite narrow, at 83 ± 10 km s^{-1}, and is offset by 258 ± 4 km s^{-1} from the optical systemic velocity (see Fig. 1). The line profile shows a broad blue-shifted component to the main peak, but it is not clear whether this is a real feature or due to the low signal-to-noise ratio of the data. Imaging of the CO line shows resolved, compact emission that is coincident with the quasar positions (see Fig. 7).

3 LENS MODELLING

Our lens modelling analysis is adapted from the grid-based modelling technique of Vegetti & Koopmans (2009). The technique simultaneously optimises for the parameters of the lens galaxy mass distribution and the source surface brightness to produce a pixellated reconstruction of the source. This method is appropriate for optical or infrared images. However, interferometers do not measure the sky surface brightness distribution directly, but measure complex 'visibilities' in the Fourier (*uv*) plane. Imaging interferometric data is a non-linear process, and the resulting image fidelity can depend heavily on the sparsity of the *uv*-plane coverage and choice of deconvolution method (e.g. CLEAN, Högbom 1974).

These systematic uncertainties can be overcome by performing model fitting on the visibility data directly. This approach has been extended to lens modelling, with parametric source models (e.g. Hezaveh et al. 2013; Bussmann et al. 2013, 2015) and also pixellated sources (e.g. Rybak et al. 2015a,b; Hezaveh et al. 2016; Dye et al. 2018). However, these frameworks are limited by the size of the data and require averaging in time and/or frequency in order to be computationally tractable. Recently, Powell et al. (2020) introduced several algorithmic improvements to overcome this limitation and model large interferometric data sets directly. We employ this method for optimising the visibility-plane posterior probability and source-plane regularisation.

Under the assumption of a smooth mass distribution, we parameterise the primary lens potential as a singular power-law ellipsoid with external shear, i.e. $\rho(r) \propto r^{-\zeta}$ (Kormann et al. 1994). For all objects, with the exception of HS 0810+2554, we perform the

model optimisation on the continuum data. For HS 0810+2554, we perform the lens modelling with the integrated CO (3–2) spectral line, which provides more extended emission and a higher signal-to-noise ratio than the continuum.

The lens redshifts are not known for HS 0810+2554, H1413+117 or WFI J2026−4536. However, the lens redshift only scales the angular size and mass of the perturber, so the inferred properties of the source are not affected.

Robust lens models have been produced for PG 1115+080 and WFI J2033−4723, based on higher quality optical imaging of the quasars and extended arcs as part of the H$_0$ Lenses in COSMO-GRAIL's Wellspring (H0LiCOW) project (Chen et al. 2019; Rusu et al. 2020). Therefore, in these cases we keep the lens slope, ellipticity and position angle fixed to literature values, and re-optimise only the lens galaxy position (which is not observed in our data) and shear parameters (for which we do not consider second-order corrections). In all other cases, we assume isothermal mass distributions (i.e. $\zeta = 2$) and optimise for the lens galaxy position, ellipticity parameters and external shear parameters.

For WFI J2033−4723, our lens model also includes a luminous satellite galaxy close to the Einstein radius of the primary lens and a massive galaxy 4 arcsec from the primary lens, both of which we parameterise as a single isothermal sphere (SIS). We find the source size changes by ≥10 percent with the addition of these galaxies, so it is necessary to explicitly include them in our model. The position and mass of these galaxies are fixed to the values found by Rusu et al. (2020). The lensing galaxy of RX J0911+0551 also has a small satellite, however this is well within the Einstein radius and we find it does not have a significant effect on our lens modelling.

The uncertainties on the lens model parameters were obtained from the posterior distributions derived using MultiNest (Feroz et al. 2013), with the source regularisation constant fixed to the maximum a posteriori value. Flat prior ranges were assumed for each free parameter, typically ±20 percent of the optimised values. For WFI J2026−4536, it was necessary to keep the lens position fixed to the maximum a posteriori (consistent within 20 mas of the optical position) for stability during the nested sampling. The likelihood-weighted posterior probability distributions for the lens parameters are given in Table 3.

Reconstructed velocity cubes were generated from the spectral line data by optimising for the source regularisation, using the best fit lens model. For WFI J2033−4723 and SDSS J0924+0219, we use only three velocity channels and restrict the *uv* data to within a maximum baseline of 300 m to improve the surface brightness sensitivity.

4 RESULTS

In this section, we present the results of the source reconstruction and an analysis of their physical properties.

4.1 Source reconstructions

The maximum a posteriori lens models are shown in Figs. 4 to 3 of the Appendix. The residual maps are a dirty image produced after the model has been subtracted from the visibility data, normalised to the rms noise in the data. We find our lens models fit the data well and the residual surface brightness features are below the 4 σ level.

The reconstructed sources and moment maps are shown in
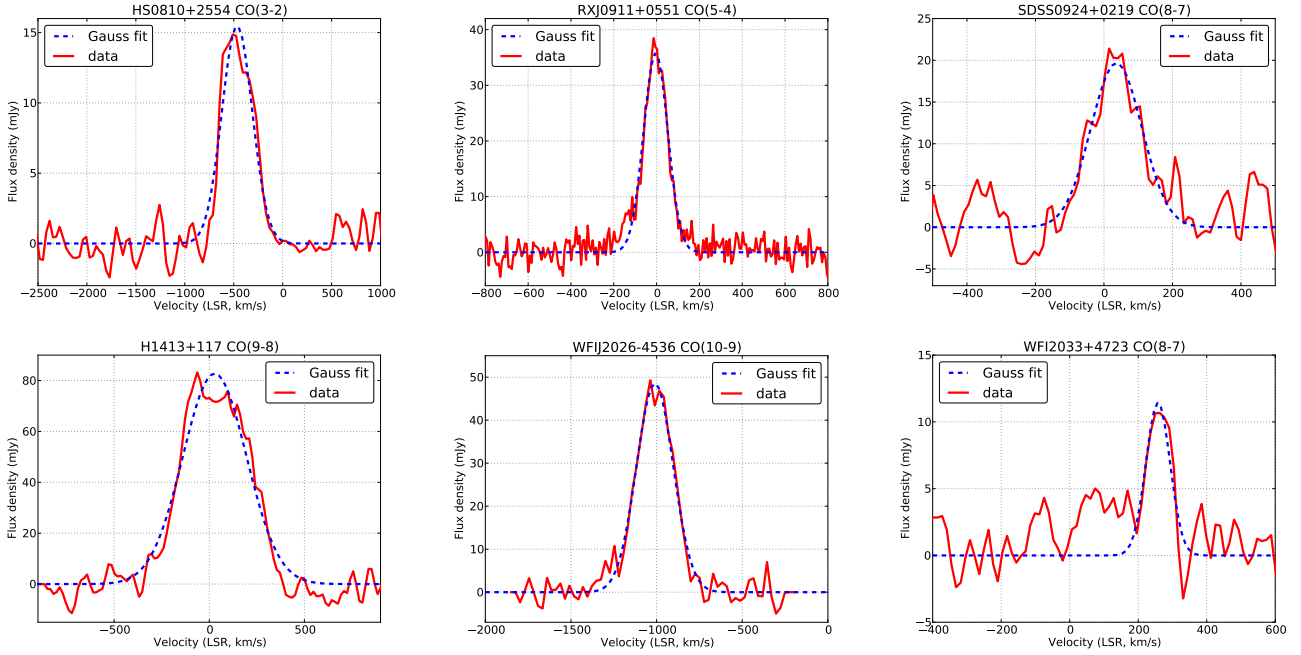
Figure 1. Line profiles for the six objects with CO observations. The red line shows the data; the blue dotted line is a Gaussian fit to the data. The systemic velocity is relative to the best redshift from the literature, using the radio definition of velocity.

Table 2. Summary of the continuum and line measurements. ν_{line} is the rest frequency of the CO line. No CO line was observed for PG 1115+080. We derive the FWHM and redshift of the CO line emission based on a single Gaussian fit to the observed line profile (see Fig. 1). Here, we give flux densities and luminosities *uncorrected* for the lensing magnification: values corrected for the lensing magnification are presented in Tables 4 and 5.

|	S_{cont} (mJy)	line	FWHM (km s^{-1})	I_{CO} (Jy km s^{-1})	L_{CO} ($L_{\odot}$)	L'_{CO} (K km s^{-1} pc^2)	z_{CO}
HS 0810+2554	0.30 ± 0.04	CO (3–2)	370 ± 10	6.0 ± 0.2	$(4.9 \pm 0.2) \times 10^8$	$(3.0 \pm 0.1) \times 10^{11}$	1.50849 ± 0.00005
RX J0911+0551	1.35 ± 0.02	CO (5–4)	133 ± 3	4.9 ± 0.1	$(4.4 \pm 0.1) \times 10^8$	$(7.2 \pm 0.1) \times 10^{10}$	2.79607 ± 0.00002
SDSS J0924+0219	9.5 ± 0.2	CO (8–7)	180 ± 10	4.1 ± 0.3	$(8.9 \pm 0.6) \times 10^8$	$(3.5 \pm 0.3) \times 10^{10}$	1.52495 ± 0.00004
PG 1115+080	2.6 ± 0.1	–	–	–	–	–	
H1413+117	26.0 ± 0.6	CO (9–8)	394 ± 8	32.0 ± 1.6	$(5.5 \pm 0.3) \times 10^9$	$(1.5 \pm 0.1) \times 10^{11}$	2.55784 ± 0.00004
WFI J2026−4536	28.31 ± 0.02	CO (10–9)	252 ± 7	15.2 ± 0.4	$(1.84 \pm 0.05) \times 10^9$	$(3.8 \pm 0.1) \times 10^{10}$	2.21217 ± 0.00003
WFI J2033−4723	10.4 ± 0.3	CO (8–7)	83 ± 10	1.0 ± 0.1	$(2.1 \pm 0.2) \times 10^8$	$(8.2 \pm 0.8) \times 10^9$	1.6629 ± 0.0002

Figs. 9 to 15. For SDSS J0924+0219 and WFI J2033−4723, the dust emission is extended and resolved into clumpy features on kpc-scales. For HS 0810+2554, RX J0911+0551, PG 1115+080, H1413+117 and WFI J2026−4536, the reconstructed dust emission appears to be very compact and does not show evidence for clumpy features on the same scales. We caution that, for HS 0810+2554, there may be extended dust emission that is not detected here due to the low signal-to-noise ratio of the data. The apparent smoothness of the compact systems may be due to angular resolution limitations, however, we note that other unlensed dusty galaxies at $z \sim 2$ are found to have smooth dust distributions (e.g. Falgarone et al. 2017). The radially averaged surface brightness distributions of the reconstructed continuum sources are shown in Fig. 17.

The robustness of the reconstructed surface brightness distribution of the lensed source depends on the quality of the data. As our source is non-parametric, our fitting down to the level of the noise can allow correlated noise features in the dirty image to be absorbed into the source reconstruction. Our investigations find that the uncertainties in the source surface brightness resulting from

noise artefacts are significantly larger than the uncertainties due to the lens model parameters (Rizzo et al. in prep). To estimate these uncertainties we assume our maximum a posteriori source model and create mock data with 100 different realisations of the noise at the level measured in the real data[1]. We create reconstructions of these mock data sets and measure the mean and standard deviation of the surface brightness in each pixel (in each channel, for spectral line data). This allows us to discriminate features in the reconstructed source from noise artefacts.

To estimate the uncertainty on the source size, we fit a Sérsic profile (Sérsic 1963) to each realisation of continuum and total line emission using a basin-hopping optimisation algorithm within the SciPy package (Wales & Doye 1998; Jones et al. 2001). For the integrated line emission of SDSS J0924+0219 and WFI J2033−4723, we fix the index of the Sérsic profile to that found for the continuum

---

[1] We find that 100 realisations is sufficient to produce a smooth distribution that can be approximated by a Gaussian function.
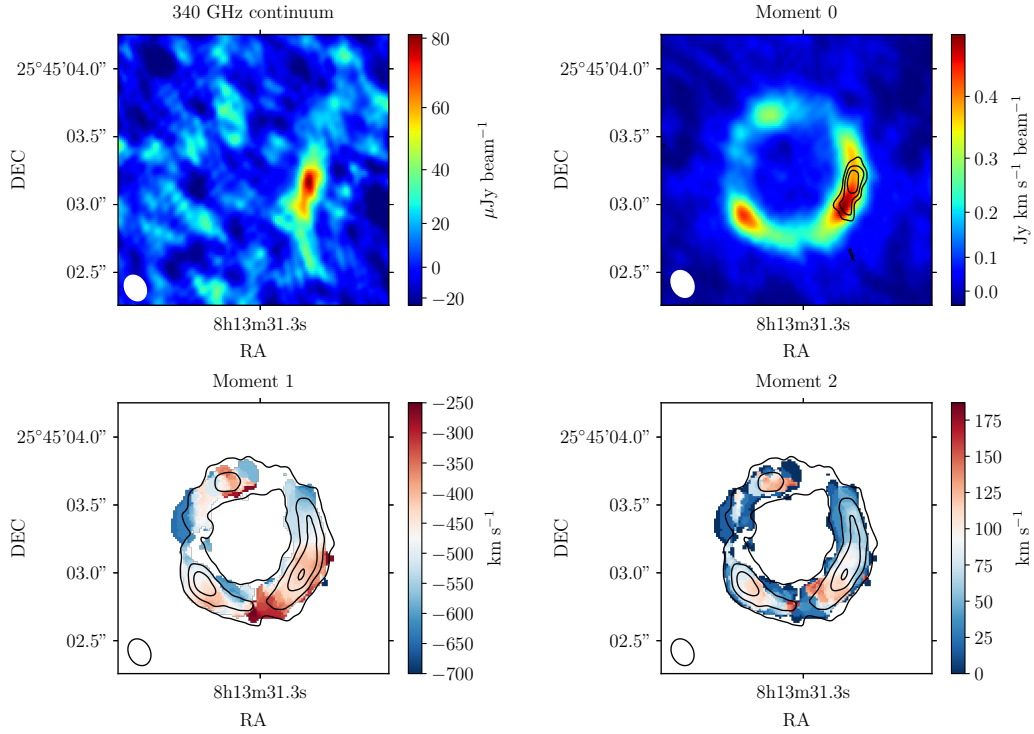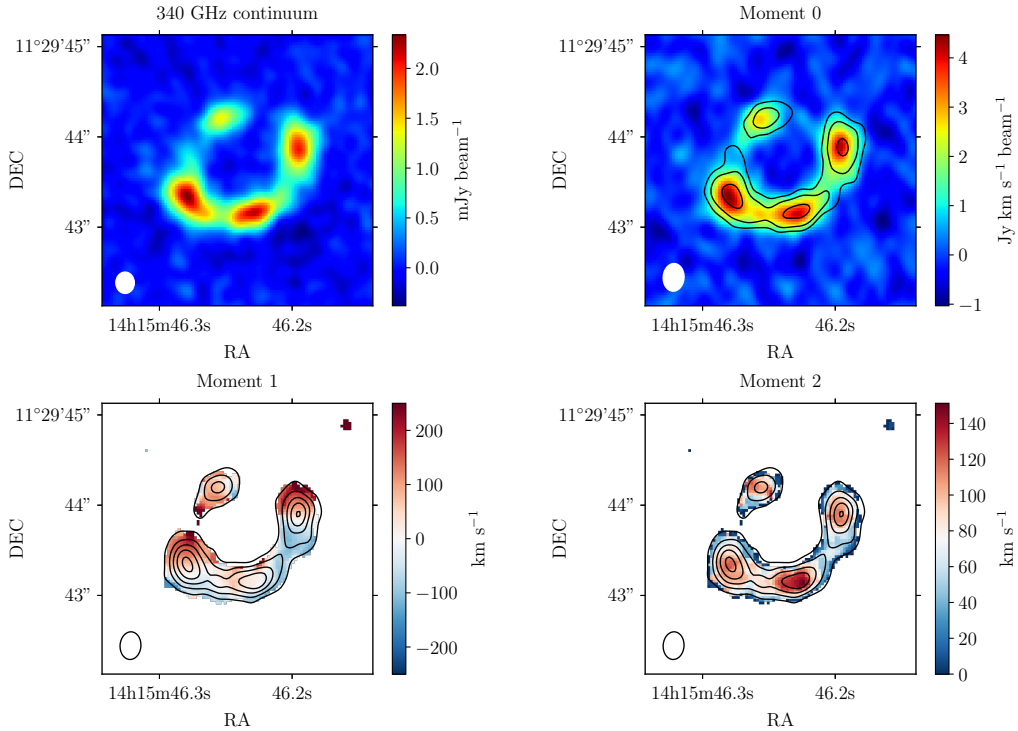
Figure 2. ALMA continuum and CO (3–2) spectral line images of HS 0810+2554. Top row: continuum image with natural weighting; moment 0 image of CO (3–2) image with contours of the continuum emission. Bottom row: moment 1 and moment 2 images, created by masking channel pixels below 4σ, overlaid with contours of the line intensity. The synthesised beam FWHM is shown in the bottom left-hand corner.
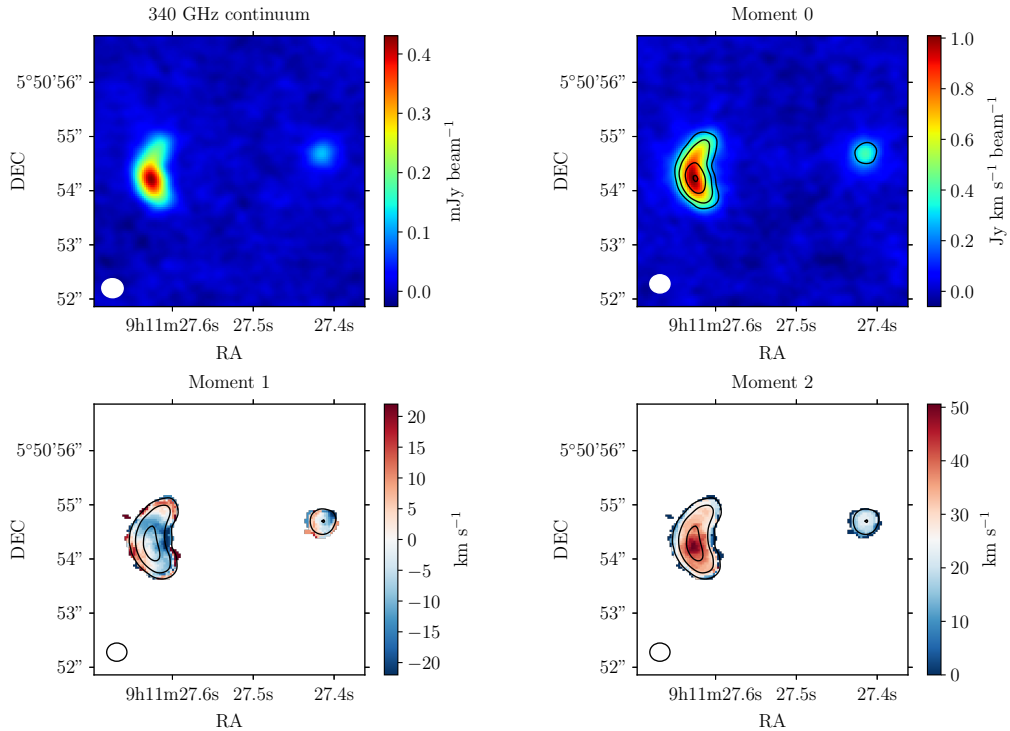
Figure 3. ALMA continuum and CO (5–4) spectral line images of RX J0911+0551. Top row: continuum image with natural weighting; moment 0 image of CO (5–4) overlaid with contours of the continuum emission. Bottom row: moment 1 and moment 2 images, made by masking channel pixels below 5σ, overlaid with contours of the line intensity. The synthesised beam FWHM is shown in the bottom left-hand corner.
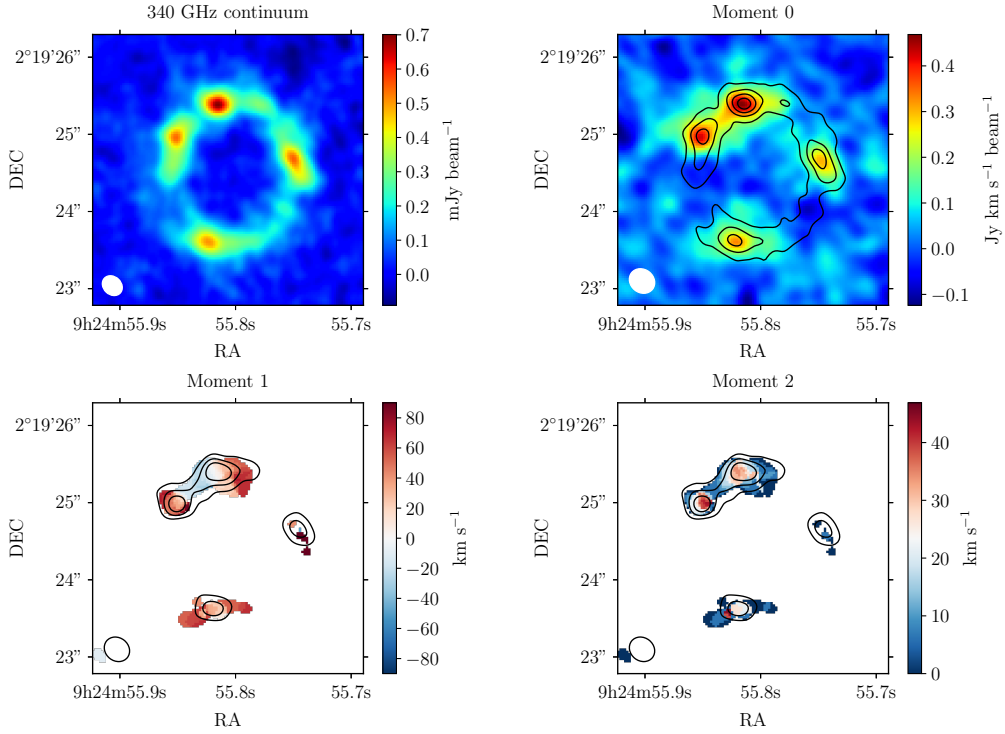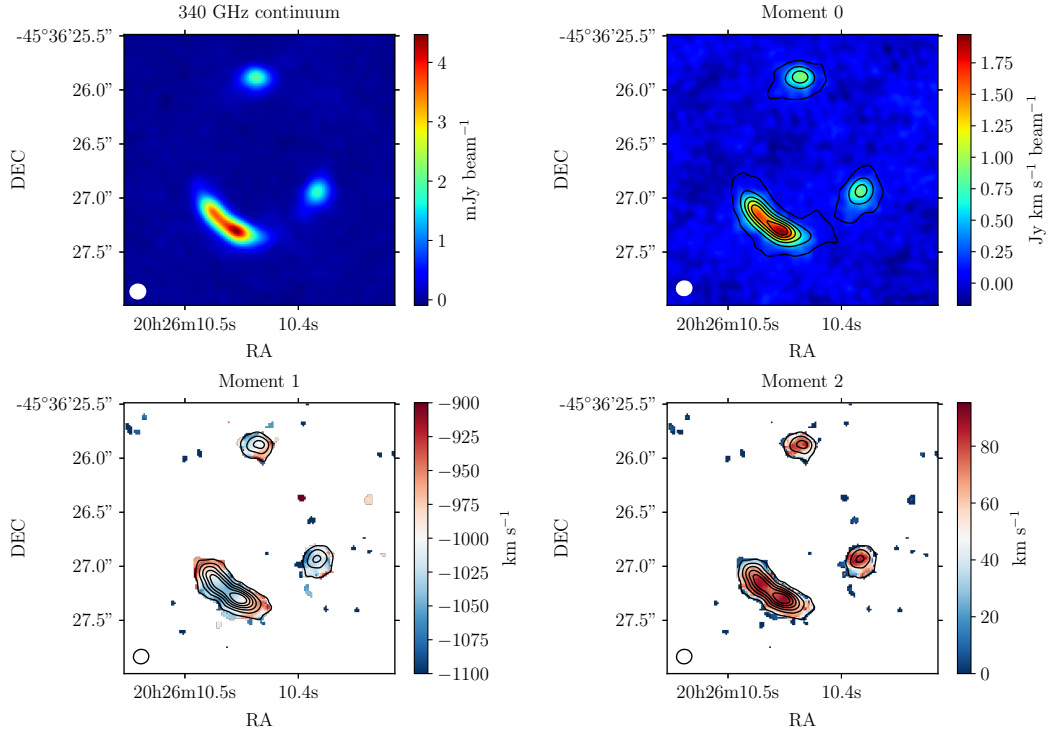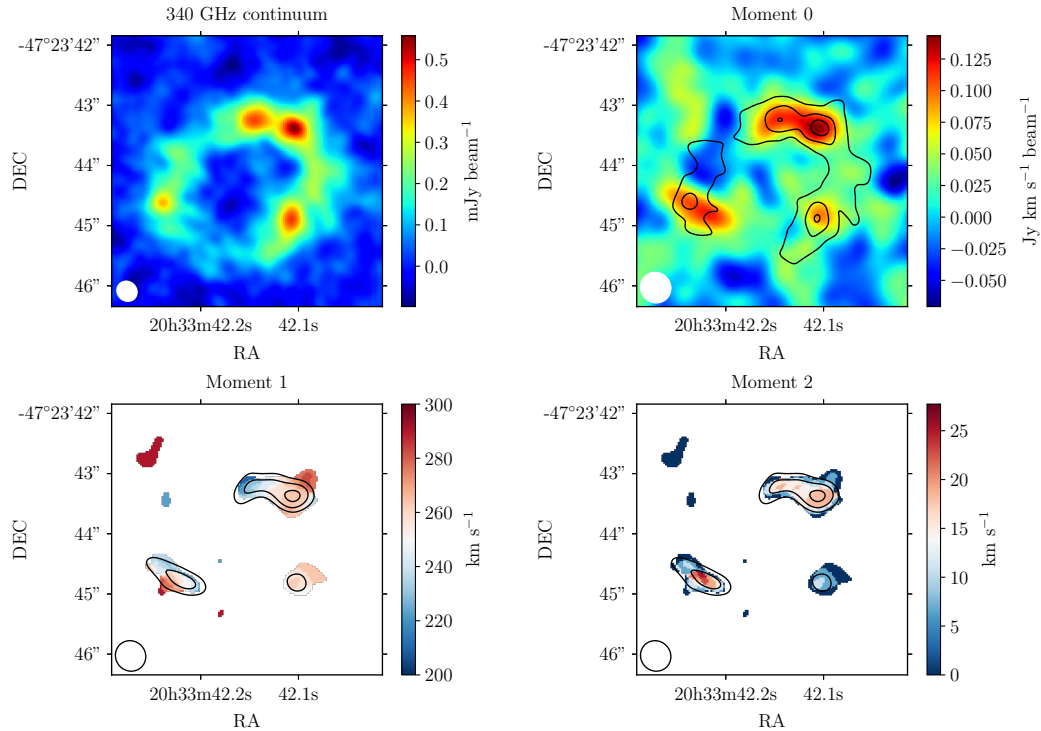
Figure 4. ALMA continuum and CO (8–7) spectral line images of SDSS0924+0219. Top row: 358 GHz continuum image with natural weighting; moment 0 image of CO (8–7) made with a uv-taper equivalent to 0.3 arcsec, overlaid with contours of the continuum emission. Bottom row: moment 1 and moment 2 images, made by masking channel pixels below 4σ, overlaid with contours of the line intensity. The synthesised beam FWHM is shown in the bottom left-hand corner.


Figure 5. ALMA continuum and CO (9–8) spectral line images of H1413+117. Top row: 290 GHz continuum image with natural weighting of the visibilities; moment 0 image of CO (9–8) image with Briggs weighting, overlaid with contours of the continuum emission. Bottom row: moment 1 and moment 2 images, made by masking channel pixels below 4σ, overlaid with contours of the line intensity. The synthesised beam FWHM is shown in the bottom left-hand corner.

Figure 6. ALMA continuum and CO (10–9) spectral line images of WFI J2026−4536. Top row: 345 GHz continuum image with natural weighting; moment 0 image of CO (10–9) overlaid with surface brightness contours of the continuum emission. Bottom row: moment 1 and moment 2 images, made by masking channel pixels below 4σ, overlaid with surface brightness contours of the line intensity. The synthesised beam FWHM is shown in the bottom left-hand corner.

Figure 7. ALMA continuum and CO (8–7) spectral line images of WFI J2033−4723. Top row: 345 GHz continuum image with natural weighting; moment 0 image of CO (8–7) made with a uv-taper equivalent to 0.4 arcsec, overlaid with surface brightness contours of the continuum emission. Bottom row: moment 1 and moment 2 images, made by masking channel pixels below 3σ, overlaid with surface brightness contours of the line intensity. The synthesised beam FWHM is shown in the bottom left-hand corner.
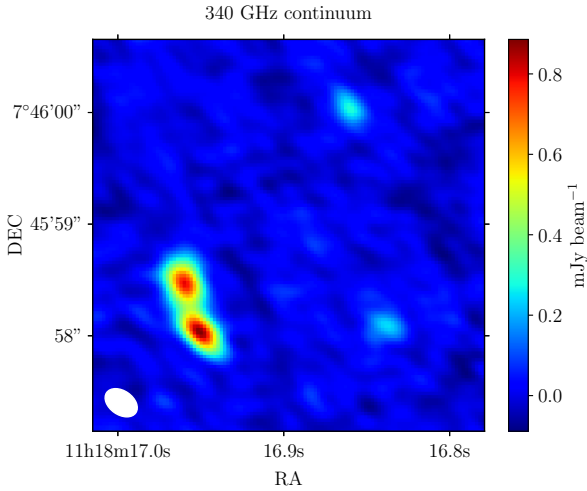
Figure 8. ALMA 346 GHz continuum images of PG 1115+080 with natural weighting of the visibility data. The synthesised beam FWHM is shown in the bottom left-hand corner.

as the fitting was found to be unstable due to the low signal-to-noise ratio of the data. We assume the mean and standard deviation of the inferred Sérsic parameters as the inferred value and its uncertainty.

For PG 1115+080, RX J0911+0551, HS 0810+2554 (continuum), SDSS J0924+0219 (line) and WFI J2033−4723 (line) the lensed emission is only marginally resolved in the tangential direction, and not at all in the radial direction. This results in a reconstructed source that appears flattened, as the size of the source in one dimension is constrained only by the angular resolution of the data. In these cases, we assume the minor axis as a more accurate estimate of the source size.

A further consequence of the lack of radial resolution is that there is a strong degeneracy between the normalised convergence (κ_0) and the slope of the lens mass density profile (ζ). The effect of this degeneracy is a geometric scaling of the reconstructed source. We assume an isothermal profile for our lens models (i.e. $\zeta \equiv 2$), however the empirical scatter in the total mass slope of early-type galaxies (0.16; Auger et al. 2010) implies an additional uncertainty in the source size. We tested this by modelling PG 1115+080 with a profile fixed to a value $\pm 1\sigma$ from the median found by Auger et al. (2010). We find that the size and normalisation of a Sérsic fit to the reconstructed source changes by ≤ 10 percent. Therefore, where we assume only an isothermal profile is fit to the data, we propagate an additional ± 10 percent error into the uncertainty in our estimated sizes to account for the empirical scatter in ζ.

We estimate the magnification of each lens system by generating a model for the lensed emission for each realisation, where source pixels are masked below a signal-to-noise ratio of 4. This value is chosen so as not to include any noise features that may be present in the individual realisations that may bias the magnification to lower values. We take the mean and standard deviation of the magnifications as the inferred value and its uncertainty (given in Tables 4 and 5).

All the derived parameters of the continuum and line emission for each source can be found in Tables 4 and 5, respectively. Note that the given magnifications are *mean* magnifications, as the magnification changes across the source and between velocity channels.

4.2 Dust properties

We use the new sub-mm data to refine the spectral energy distribution (SED) models for our sample. The SED fitting follows a similar procedure described by Stacey et al. (2018) and uses ancillary data listed therein. Stacey et al. (2018) assumed the case of optically thin dust emission. However, there is growing evidence that an optically thin dust model under-predicts the dust temperature of high-redshift galaxies because the dust remains optically thick into the far-infrared (Riechers et al. 2013, Cortzen et al. 2020). This difference has little effect on the SED shape (hence, integrated luminosity) but shifts the peak of the dust emission to longer wavelengths, such that warmer dust temperatures can appear colder (by a few degrees, on average). Therefore, we fit a dust model described by

$$S_\nu \propto (1 - e^{\nu/\nu_0}) \frac{\nu^3}{e^{h\nu/kT_d} - 1}, \quad (1)$$

where ν_0 is the frequency at which the dust opacity is unity, which we assume to be rest-frame 3 THz (100 μm) as predicted by theory (Draine 2006) and supported by observational studies (Riechers et al. 2013).

We leave both the dust temperature and emissivity (which governs the steepness of the Rayleigh-Jeans slope of the spectrum) as free parameters. Depending on the available ancillary data, we also fit a power-law component described by

$$S_\nu \propto \nu^\alpha, \quad (2)$$

where α is the spectral index, to account for optically thin radio synchrotron emission.

We apply a Markov Chain Monte Carlo (MCMC) analysis using the Python implementation EMCEE (Foreman-Mackey et al. 2013) to infer the marginalised posterior distributions for each free parameter and the integrated FIR luminosity. The SED models are shown in Figs. 1 and 2 of the Appendix. The parameters from the SED modelling, corrected for the lensing magnification, are listed in Table 4.

The dust temperature we infer from our SED fitting is an *effective* dust temperature, which should not be considered a true measure of dust temperature, but weighted by multiple components of dust emission. This may include a cold dust component from cirrus dust of the interstellar medium (~ 20 K) and a warmer dust component associated with star-forming regions (~ 50 K). Indeed, Swinbank et al. (2014) find DSFGs require at least three dust components to account for the full mid-infrared (MIR) to FIR SED. AGN host galaxies may also have contributions from AGN-heated dust emission. For HS 0810+2554 and H1413+117, we account for a warm dust component, which we assume is associated with the AGN. For HS 0810+2554, β is kept fixed in the SED modelling as we do not have sufficient data points to fit both β and two dust components. We fix β to a value of 2, as 1.5 cannot produce a satisfactory fit to the data[2]. With the exception of H1413+117 and HS 0810+2554, we do not have data at rest-frame wavelengths ~ 10 to 100 μm to consider additional dust emission components.

Note that, while we leave β as a free parameter, its value is not necessarily physically significant as, for poorly sampled SEDs, the strong temperature–β degeneracy absorbs the observational noise in the data (Juvela & Ysard 2012). We allow this as a free parameter

---

[2] For comparison, the median and distribution of the parent sample is $\beta = 2.0^{+0.4}_{-0.5}$, based on optically thin dust models (Stacey et al. 2018).
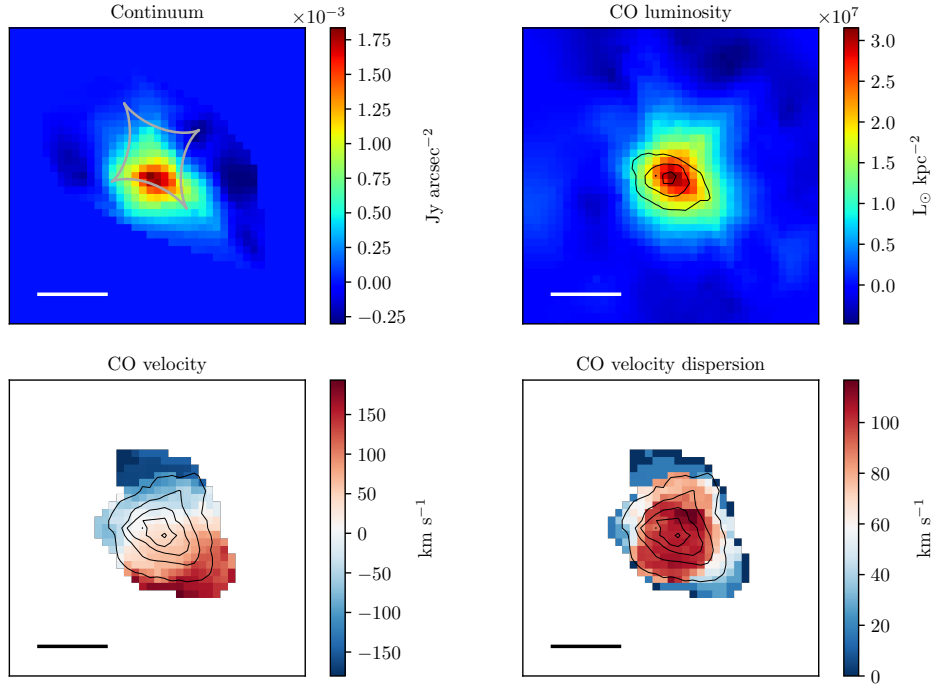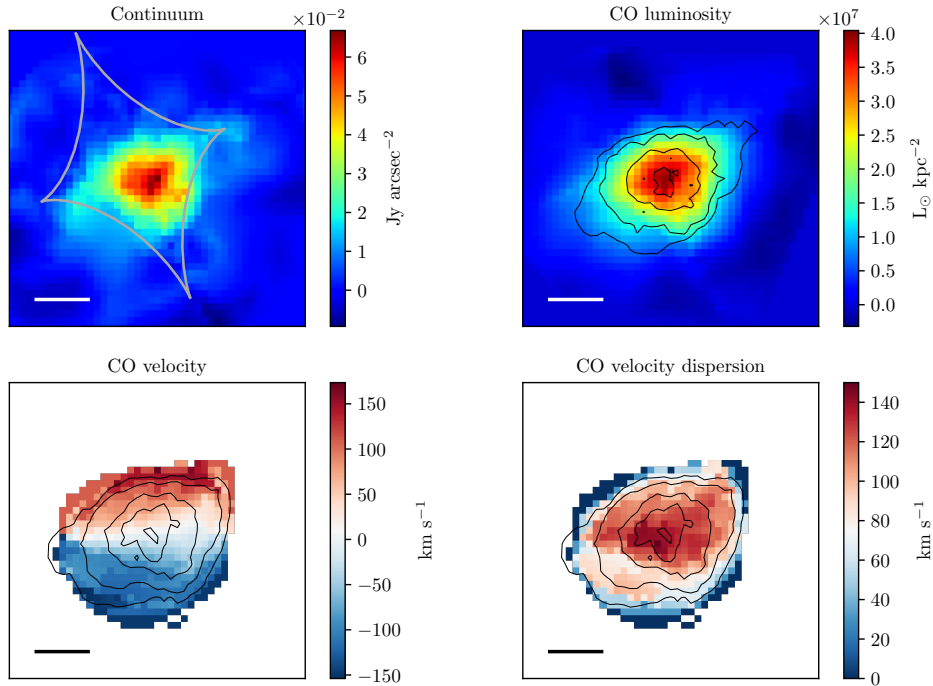
Figure 9. Reconstructed dust and CO (3–2) spectral line emission of HS 0810+2554. The continuum dust emission is shown in units of Jy arcsec^{-2} with the lensing caustics shown in grey. The moment 0 image is overlaid with continuum signal-to-noise ratio contours of 3, 4 and 5 based on the error analysis. The moment 1 and 2 images are overlaid with signal-to-noise ratio contours of the line intensity (3 and multiples of 5). The line reconstructions are generated by masking pixels in each channel below 3σ. The bar shows 1 kpc at the redshift of the source. The CO velocity is corrected to the redshift derived from a Gaussian fit to the CO line profile.
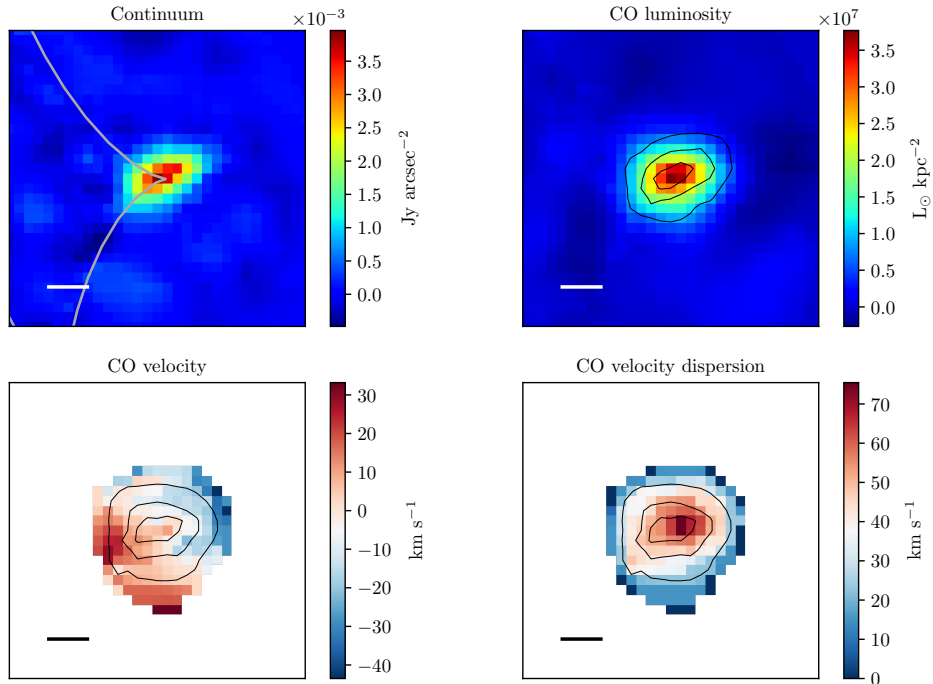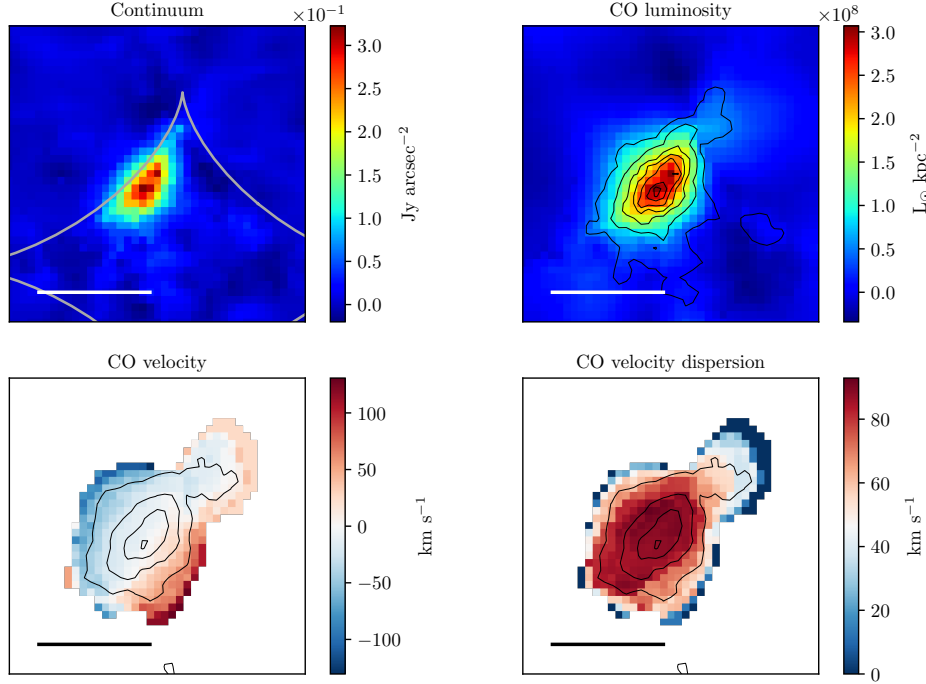

Figure 10. Reconstructed dust and CO (5–4) spectral line emission of RX J0911+0551. The continuum dust emission is shown in units of Jy arcsec^{-2} with the lensing caustics shown in grey. The moment 0 image is overlaid with the signal-to-noise ratio contours of the continuum (3 and multiples of 5). The moment 1 and 2 images are overlaid with signal-to-noise contours of the line intensity (3 and multiples of 5). The line reconstructions are generated by masking pixels in each channel below a signal-to-noise ratio of 3. The bar shows 1 kpc at the redshift of the source. The CO velocity is corrected to the redshift derived from a Gaussian fit to the CO line profile.
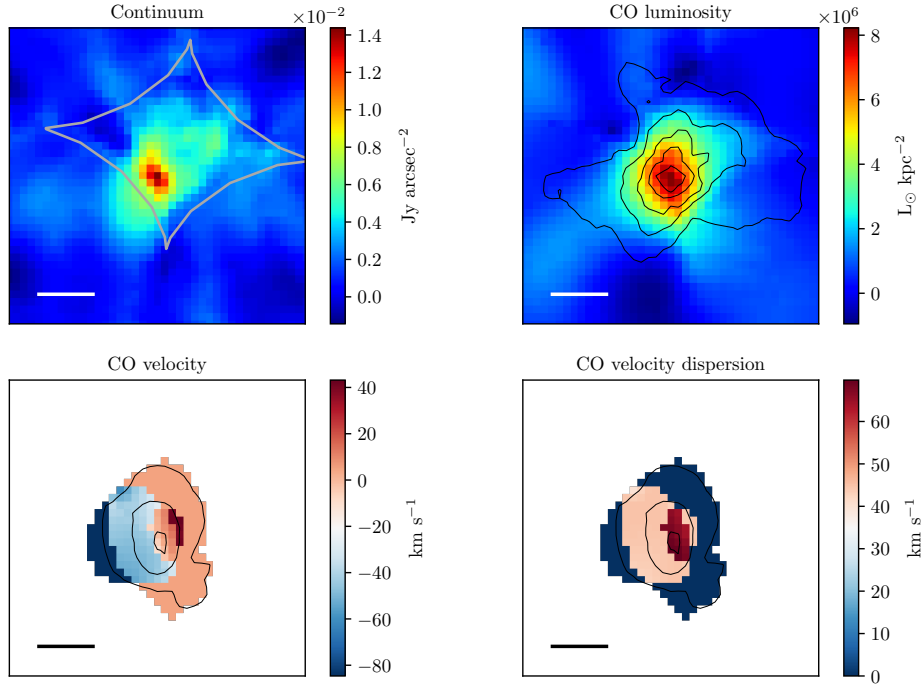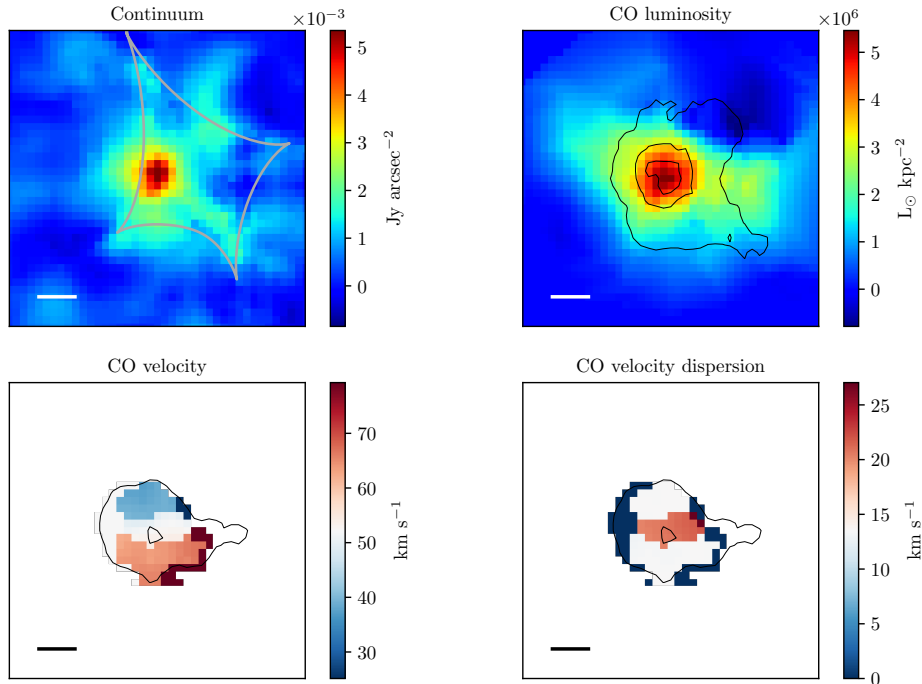
Figure 11. Reconstructed dust and CO (8–7) spectral line emission of SDSS J0924+0219. The dust emission is shown in units of Jy arcsec^{-2} with the lensing caustics shown in grey. The moment 0 image is overlaid with signal-to-noise ratio contours of the continuum, in steps of 3. The moment 1 and 2 images are overlaid with signal-to-noise ratio contours of the line intensity in steps of 3. The line reconstructions are generated by masking pixels in each channel below a signal-to-noise ratio of 3. The bar shows 1 kpc at the redshift of the source. The CO velocity is corrected to the redshift derived from a Gaussian fit to the CO line profile.

Figure 12. Reconstructed dust and CO (9–8) spectral line emission of H1413+117. The dust emission is shown in units of Jy arcsec^{-2}. The moment 0 image is overlaid with signal-to-noise ratio contours of the continuum (3 and multiples of 5). The moment 1 and 2 images are overlaid with signal-to-noise ratio contours of the line intensity (3 and multiples of 5). The line reconstructions are generated by masking pixels below a signal-to-noise ratio of 3. The bar shows 1 kpc at the redshift of the source. The CO velocity is corrected to the redshift derived from a Gaussian fit to the CO line profile.

Figure 13. Reconstructed dust and CO (10–9) spectral line emission of WFI 2026−4536. The dust emission is shown in units of Jy arcsec^{-2} with the lensing caustics shown in grey. The moment 0 image is overlaid with signal-to-noise ratio contours of the continuum (3 and multiples of 10). The line reconstructions are generated by masking pixels in each channel below a signal-to-noise ratio of 3. The moment 1 and 2 images are overlaid with signal-to-noise ratio contours of the line intensity (3 and multiples of 10). The bar shows 1 kpc at the redshift of the source. The CO velocity is corrected to the redshift derived from a Gaussian fit to the CO line profile.


Figure 14. Reconstructed dust and CO (8–7) spectral line emission of WFI 2033−4723. The dust emission is shown in units of Jy arcsec^{-2} with the lensing caustics shown in grey. The moment 0 image is overlaid with the continuum signal-to-noise ratio contours, in steps of 3. The line reconstructions are generated by masking pixels in each channel below 3σ. The moment 1 and 2 images are overlaid with signal-to-noise ratio contours of the line intensity, in steps of 3. The bar shows 1 kpc at the redshift of the source. The CO velocity is corrected to the redshift derived from a Gaussian fit to the CO line profile.
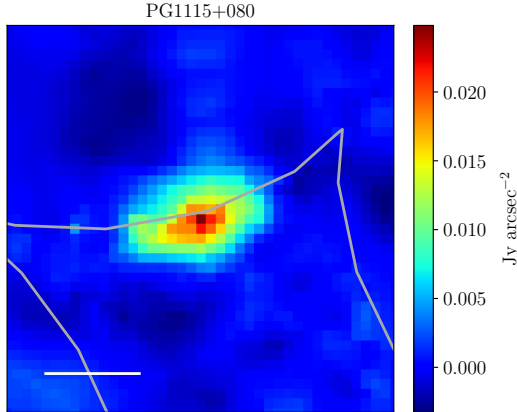
Figure 15. Reconstructed dust emission of PG 1115+080, shown in units of Jy arcsec^{-2} with the lensing caustics shown in grey. The white bar shows 1 kpc at the redshift of the source.

to better estimate the true uncertainty on the fitted temperature and luminosity.

We follow the Helou et al. (1988) definition of FIR luminosity ($L_{\rm FIR}$), as the integrated spectra from 40 to 120 μm. We convert this to total infrared luminosity (8 to 1000 μm) using a colour correction factor of 1.91 (i.e. $L_{\rm IR} = 1.91 \times L_{\rm FIR}$) given by Dale et al. (2001) to account for spectral features in the MIR, assuming our fitted cold dust component is associated only with obscured star formation. We convert this to a star formation rate (SFR; M$_\odot$ yr^{-1}) assuming a Salpeter initial mass function with the conversion factor of Kennicutt (1998),

$$SFR = \frac{L_{\rm IR}}{5.8 \times 10^9},\tag{3}$$

where $L_{\rm IR}$ is in units of L$_\odot$[3]. Using these inferred star formation rates and magnifications, we transform the dust emission to units of star formation rate surface density. For four host galaxies with resolved structure, the star formation rate surface densities are shown in Fig. 16.

We follow Dunne et al. (2000) to estimate the dust mass from our SED fits using

$$M_{\rm dust} = \frac{D_{\rm L}^2\, S_{850}^{\rm obs}}{(1+z)\,\kappa_{850}\,B_{850}(T_{\rm d})},\tag{4}$$

where $S_{850}^{\rm obs}$ is the observed flux density at rest-frame wavelength 850 μm (350 GHz), $D_{\rm L}$ is the luminosity distance, κ_{850} is the dust mass opacity (0.077 m^2 kg^{-1}, from Dunne et al. 2000), and $B_{850}(T)$ is the value of a black body of temperature T at 850 μm.

It has often been found that a dust mass estimated from single temperature SED model may underestimate the total dust content, as most of the mass is in cold cirrus dust and not the dust

---

[3] Note that there is evidence that starbursts have top-heavy IMFs (Zhang et al. 2018). Our assumption of a Salpeter IMF may overestimate the star formation rate by overestimating the number of low-mass stars; thus, a different choice of IMF would result in an overall re-scaling of the star formation rates. However, as we are mostly concerned with *relative* star formation rates in this work, our choice of IMF does not significantly impact our results.

that contributes most to the effective (luminosity-weighted) temperature (e.g. Scoville et al. 2014). However, there is also evidence that multi-component dust models could lead to overly large dust masses (Cortzen et al. 2020) and it has not been established to what extent the approach is appropriate for quasar host galaxies. Note that, if the temperature of dust in the diffuse ISM is much lower than the effective dust temperature for quasar hosts, the dust masses derived for of our sample could be underestimated. We attempted fitting two-component models to our SEDs but, as most are sparsely sampled, the uncertainties on the mass of the cold component was very large and encompasses the masses derived with a single temperature fit. Thus, we report the dust masses from a single-temperature fit, but with this caveat.

The dust temperatures, emissivities, intrinsic luminosities, star formation rates, star formation rate surface densities and dust masses for the sample are given in Table 4. For H1413+117, the nearby field source we identify in our ALMA imaging (Section 2.6) may cause modest confusion in SED fitting, which leads to overestimates of the inferred star formation properties of the source of interest. Photometric measurements at multiple frequencies will be required to accurately de-blend this emission from the total infrared luminosity. Such an analysis is beyond the scope of this work, however, the consistent relative flux density of the objects at 100 and 290 GHz suggests that the neighbour contributes ∼ 20 percent to the photometry of H1413+117. Therefore, our measurements based on infrared luminosity are likely to be overestimated by a similar percentage. We estimate the effect of this by scaling all the photometric measurements above 300 GHz by a factor of 0.8. The physical properties based on the re-scaled data are also shown in Table 4.

4.3 Molecular gas properties

Fig. 18 shows the intrinsic effective radius of the dust and CO emission against effective dust temperature and total infrared luminosity (8–1000 μm). The sample in this work is quite heterogeneous and different rotational transitions of CO were observed. These CO lines correspond to different physical conditions in the ISM. At one extreme, CO (10–9), CO (9–8) and CO (8–7) trace warm gas (150–200 K) in regions of intense star formation or that are associated with AGN. For the four objects where we observe one of these lines (SDSS J0924+0219, H1413+117, WFI J2026−4536 and WFI J2033−4723), the molecular gas is the same size or more compact than the dust continuum. For HS 0810+2554 and RX J0911+0551, in which we observe CO (5–4) and CO (3–2), which are usually associated with star-forming regions, we find the gas to be more extended than the dust. Different relative sizes of the emission regions of CO line transitions have been found for other DSFGs (e.g. Apostolovski et al. 2019). While little can be inferred about the relative contributions to the energy budget from observations of a single line transition, the observed sizes are consistent with high levels of star formation and with the expectations for a radially decreasing gas column density and temperature (Weiß et al. 2007).

We convert our line flux densities to luminosities ($L_{\rm CO}$ and $L'_{\rm CO}$) with relations as given by Solomon & Vanden Bout (2005). We use the source-plane reconstructions to derive the intrinsic line properties to account for differential magnification across the velocity channels. As some line velocity components may be more strongly magnified than others, the integrated line emission measured in the lens-plane is not necessarily the same as the intrinsic line emission multiplied by the mean magnification (i.e. $I_{\rm CO}^{\rm lensed} \neq \bar{\mu} \times I_{\rm CO}$). The intrinsic line luminosities (corrected for lensing mag-
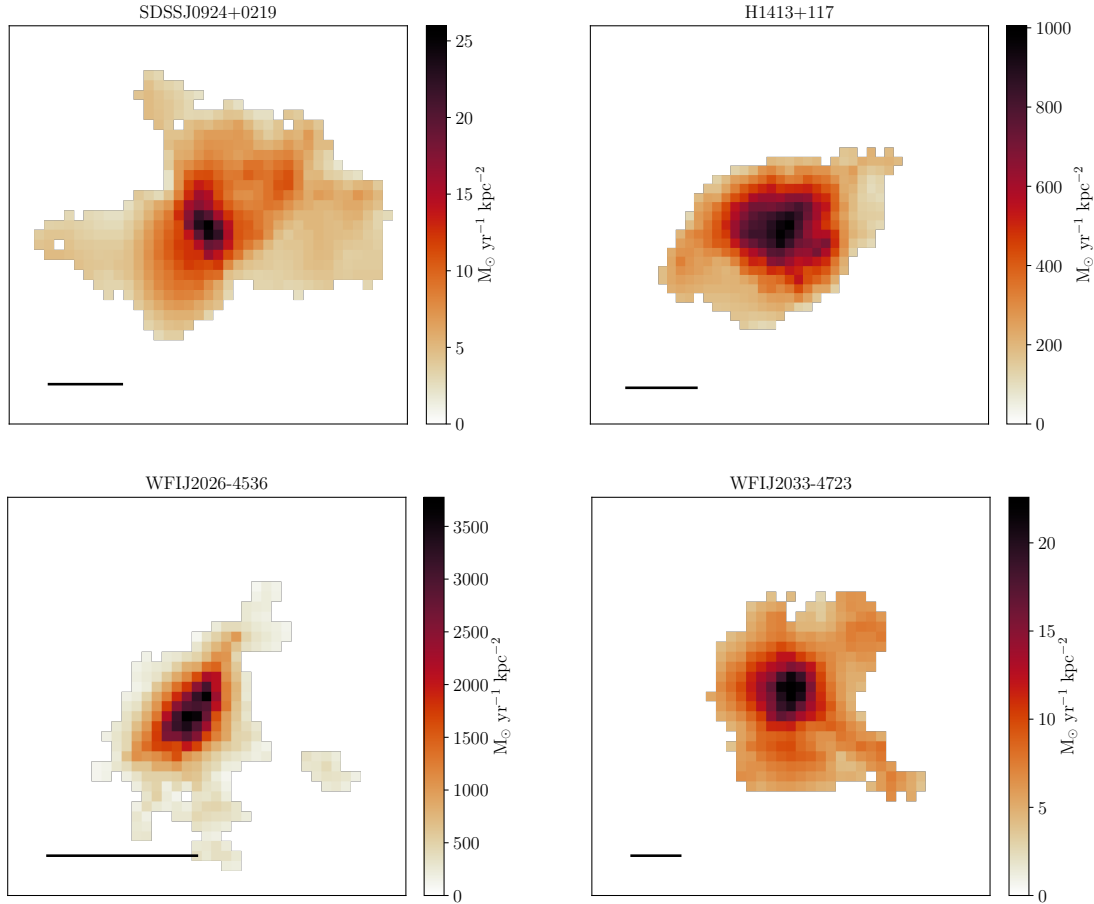
Figure 16. Reconstructed star formation rate surface density of SDSS J0924+0219, H1413+117, WFI J2026−4536 and WFI J2033−5723. Pixels below a signal-to-noise ratio threshold of 3 are masked. The black bar shows 1 kpc at the redshift of the source, for scale.

nification) are given in Table 5. The reconstructed line emission in units of luminosity surface density, as well as the velocity field and velocity dispersion, are shown for each source in Figs. 9 to 14.

In all cases, the reconstructed line velocity structure shows evidence of rotation around the peak of the continuum emission, suggesting the gas is in disc. From the reconstructed line emission, we estimate the enclosed dynamical mass of the galaxies, assuming

$$M_{\mathrm{dyn}} = \frac{R_{\mathrm{2eff}} V_{\mathrm{max}}^2}{G}, \quad (5)$$

where R_{2eff} is twice the effective radius of the CO emission based on the Sérsic model fit described in Section 4.1. Here, σ is the maximum rotational velocity, assuming $V_{\mathrm{max}} = V_{\mathrm{obs}}/\sin i$, where i is the inclination angle. We derive $\sin i$ from the Sérsic model fit according to

$$\sin i = \sqrt{1 - \left(\frac{b}{a}\right)^2}, \quad (6)$$

where b is the minor axis and a is the major axis. Where we do not have a reliable constraint on the axis ratio due to a lack of radial resolution (i.e. RX J0911+0551, PG 1115+080 and WFI J2033−4723) we assume an inclination angle of 45±15 deg, corresponding to axis ratios of 0.5 to 0.9. In this case, we do not consider axis ratios below 0.5 as they are smaller than the apparent axis ratio. This method

assumes that the circular velocity accurately traces the gas rotation, ignoring the effect of a non-spherical gravitational potential and turbulent pressure. Simulations suggest that this assumption could result in an underestimate of the dynamical mass at very small or large radii, but is accurate at the intermediate radii (∼ 1 kpc) we probe here (Wellons et al. 2020). The dynamical masses for the quasar hosts are given in Table 5. Note that the dynamical mass inferred from the CO lines investigated here (particularly the high-excitation lines) may not probe the total mass of the galaxy (Casey et al. 2018).

In addition to the availability of gas, the level of star formation in a galaxy depends on the local balance between turbulent pressure and self-gravity. In dynamically unstable systems, self-gravity dominates over turbulent pressure allowing gas to fragment and efficiently form stars. As the systems in this work are known to have high star formation rates and, in some cases, have clumpy non-axisymmetric dust structures, we expect the gas discs to be globally dynamically unstable. As shown in Figs. 9 to 15, the reconstructed velocity maps appear to show radially increasing rotational velocity and high central dispersions. However, these 2-dimensional maps may be strongly affected by beam-smearing, which can misguide interpretation of the dynamics of the systems (velocity dispersion in particular, e.g. Lelli, Fraternali & Sancisi 2010). Also note that for SDSS J0924+0219 and WFI J2033−4723 we use only three velocity channels for the reconstructions. We defer a 3D analysis to
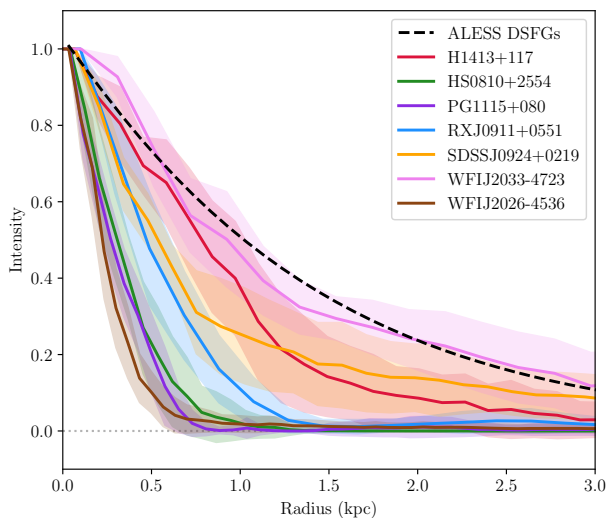
Figure 17. Normalised, azimuthally averaged surface brightness profiles of the reconstructed dust emission from the quasar hosts, accounting for ellipticity. The shaded regions show the respective standard deviation of the dust emission. The radius of HS 0810+2554, RX J0911+0551 and PG 1115+080 are scaled to the size of the minor axis, based on the axis ratio from the Sérsic model fits (see Section 4.1). The black dotted line shows the mean profile of (unlensed) ALESS DSFGs from Sérsic fits (Hodge et al. 2016, 2019).

future work, combining lens and source kinematic modelling as introduced by Rizzo et al. (2018) (see also Rizzo et al. 2020).

4.4   Comparison with dusty star-forming galaxies

We make a comparison between our lensed quasar hosts and high angular resolution ALMA observations of DSFGs. These samples include galaxies from the LABOCA ECDFS Submm Survey (ALESS; Hodge et al. 2016), strongly lensed DSFGs selected with *Herschel* surveys, and several DSFGs at $z > 4$. The choice of these samples is motivated by the different selection biases that dominate in FIR/sub-mm surveys: we choose these samples to represent a diverse range of properties observed for DSFGs and combat the effects of selection bias.

DSFGs in the ALESS sample cover a similar redshift range ($z \sim 2$, including one at $z = 3.4$) and infrared luminosities to our lensed quasar sample. We perform SED fitting for the ALESS sample with photometry from Swinbank et al. (2014) and Hodge et al. (2019). For consistency, we use the same methodology as for the quasar hosts to obtain effective dust temperatures and infrared luminosities with an optically thick dust model. Following this methodology, we only include the 11 ALESS galaxies where there are sufficient detections at FIR–sub-mm wavelengths to constrain the dust temperature.

We note that sub-mm source selection may preferentially identify sources with lower dust temperatures at a given redshift, due to the effect of negative k-correction (Chapin et al. 2011). This does not strongly influence the selection of the quasar hosts (which were mostly selected on the basis of their optical properties and lens configuration, as detailed in Section 2) but may influence the selection of the coeval DSFGs. To account for this selection bias, we include a sample of DSFGs at $z > 4$ and several lensed DSFGs. The $z > 4$ sample includes one of the ALESS DSFGs (Hodge et al. 2019) and four other objects that are spatially resolved, and have spec-

troscopic redshifts and multiple detections at FIR–sub-mm wavelengths. These include GN20 (Hodge et al. 2015), HFLS3 (Riechers et al. 2013), AzTEC-3 (Riechers et al. 2014), the two components of SGP38326 (Oteo et al. 2016) and the two components of ADFS-27 (Riechers et al. 2017). A summary of the DSFGs is given in Table 1 of the Appendix.

The lensed DSFGs were selected in FIR surveys with *Herschel*/SPIRE (Negrello et al. 2017). We perform the same analysis for the lensed DSFGs as for the lensed quasar sample; further details of the lens modelling and source reconstructions will be presented in a follow-up paper (Stacey et al. in prep). The selection of lensed DSFGs is expected to be strongly biased towards compact systems, where the flux density is boosted by high magnification (Serjeant 2012; Hezaveh et al. 2012). We therefore expect these lensed systems to be examples of more compact DSFGs.

Fig. 19 (left) shows the continuum source size (effective radius) of the quasar hosts in this work and the $z \sim 2$ DSFGs. This shows that more compact dust emission is associated with higher effective dust temperatures. A Kendall rank test (Kendall 1945) for correlation between dust size and temperature yields a coefficient of $\tau = -0.38$ with a significance of $p = 0.02$ (where $p = 0.05$ is often taken as significant). Such a relationship is expected as a natural consequence of the Stefan-Boltzmann law, which relates the luminosity of a black body to its temperature and physical size. If the luminosity and temperature of the thermal dust emission we observe from the quasar hosts is related only to star formation, they should follow this relation.

Fig. 20 shows the intrinsic infrared luminosity (and equivalent star formation rate) against effective dust temperature for our sample and the DSFGs. The relationship expected for the modified Stefan-Boltzmann law from Yan & Ma (2016) is also shown for different source sizes, assuming a dust model with $\beta = 1.5$ and $\nu_0 = 3$ THz. The DSFGs and quasar hosts can be seen to broadly follow this relationship with some scatter, as expected due to source structure as well as variations in dust emissivity and opacity. Fig. 20 shows that two lensed quasars have sizes in dust emission larger than implied by their dust temperature, which could indicate the sub-mm emission has a significant contribution from AGN-heating. However, we note that for these systems (SDSS J0924+0219 and WFI J2033−4723) the dust distribution is resolved into multiple clumps and a single Sérsic component is likely a poor descriptor of their surface brightness distribution (Figs. 11 and 14). This is also the case for some lensed DSFGs. This blending effect was also suggested by Yan & Ma (2016), who found some DSFGs have sizes in dust emission larger than expected from the Stefan-Boltzmann relation.

Fig. 20 suggests that the dust emission of quasar hosts generally have smaller sizes and higher temperatures than DSFGs of similar infrared luminosity, and smaller sizes and higher luminosities than DSFGs of similar temperature. The $z \sim 2$ sub-mm-selected DSFGs are a factor of ~ 3 larger than quasar hosts, the $z > 4$ DSFGs have intermediate sizes between the $z \sim 2$ DSFGs and quasar hosts, and lensed DSFGs span a broad range of sizes in dust emission ($0.5 < R_{\mathrm{eff}} < 3.8$) the smaller of which are similar to lensed quasars.

4.5   Intensity of star formation

We estimate the galaxy-averaged star formation rate surface density (Σ_{SFR}; $M_\odot$ yr^{-1} kpc^{-2}), for our sample and the DSFGs, assuming

$$\Sigma_{\text{SFR}} = 0.5 \times \frac{SFR}{\pi R_{\text{eff}}^2}, \qquad (7)$$

where R_{eff} is the dust effective radius based on the Sérsic model fit. Fig. 19 (right) shows the galaxy-averaged star formation rate surface density against effective radius, where the dotted tracks show the analytic relationship for $\log L_{\text{IR}}$ of 11.5, 12, 12.5, 13 and 13.5, following Eq. 7.

We estimate the optically thick Eddington flux limit (F_{Edd}) assuming the relation from Andrews & Thompson (2011) for warm starbursts,

$$F_{\text{Edd}} \sim 10^{13} \, \text{L}_\odot \, \text{kpc}^{-2} \, f_{\text{gas}}^{-1/2} \, f_{\text{dg},150}^{-1}, \qquad (8)$$

where f_{gas} is the gas fraction and $f_{\text{dg},150}$ is the dust-to-gas ratio multiplied by 150. Using a typical gas fraction of 0.5 ± 0.2 (Spilker et al. 2016) and a dust-to-gas ratio of 0.010 ± 0.005 (roughly solar metallicity), we derive an estimate of the Eddington-limited star formation rate surface density of $1600 \pm 800 \, \text{M}_\odot \, \text{yr}^{-1} \, \text{kpc}^{-2}$. As can be seen in Fig. 19, the mean star formation rate density of four quasar hosts are within a factor of 2 to 3 of the estimated Eddington limit. As this is a mean star formation rate density, the proximity to the Eddington limit may imply that at least some star formation is Eddington limited. The peak star formation rate surface densities range from 25–$3700 \, \text{M}_\odot \, \text{yr}^{-1} \, \text{kpc}^{-2}$, perhaps suggesting super-Eddington star formation in the most extreme case (WFI J2026−4536).

HS 0810+2554 is the only object where we observe CO (3–2), which is a common proxy for molecular hydrogen (H_2; Greve et al. 2014). We assume $\alpha_{\text{CO}} = 0.8 \, \text{M}_\odot \, (\text{K km s}^{-1} \, \text{pc}^2)^{-1}$, as is often assumed for dusty starbursts, to convert L'_{CO} to total gas mass (M_{gas}). For this object we find $M_{\text{gas}} = (2.1 \pm 0.1) \times 10^9 \, \text{M}_\odot$ and $\Sigma_{\text{gas}} = 1.6 \pm 0.7 \, \text{M}_\odot \, \text{kpc}^{-2}$ (derived in the same manner as Eq. 7). This implies a very low gas fraction of just 0.06 ± 0.04 compared to its dynamical mass, and a dust-to-gas ratio is 0.006 ± 0.002 (slightly below solar metallicity). The implied gas depletion timescale (i.e. $t_{\text{dep}} \equiv M_{\text{gas}}/SFR$) is 50 ± 40 Myr.

5 DISCUSSION

5.1 Evidence for extreme star formation in quasar host galaxies

The seven objects investigated here were selected from a larger survey of 104 lensed quasars with *Herschel*/SPIRE that was reported by Stacey et al. (2018), who performed SED fitting to constrain the level of dust-obscured star formation in the sample. In all but three cases (including H1413+117), a single dust component was used for the fitting due to the lack of data in the MIR to FIR. From this analysis, Stacey et al. (2018) found a median dust temperature of 38^{+12}_{-5} K (based on optically thin dust models) and a median star formation rate of $120^{+160}_{-80} \, \text{M}_\odot \, \text{yr}^{-1}$, both of which are typical of DSFGs. A concern from such a simple SED model is that AGN-heated dust emission could contribute to the FIR and result in a higher dust temperature and, hence, a higher effective dust temperature (e.g. Kirkpatrick et al. 2012). Indeed, in some cases, effective dust temperatures were found that are higher than typical for star formation. However, we find that the quasar hosts are generally consistent with the Stefan-Boltzmann relation between temperature and luminosity when considering an optically thick dust model (see
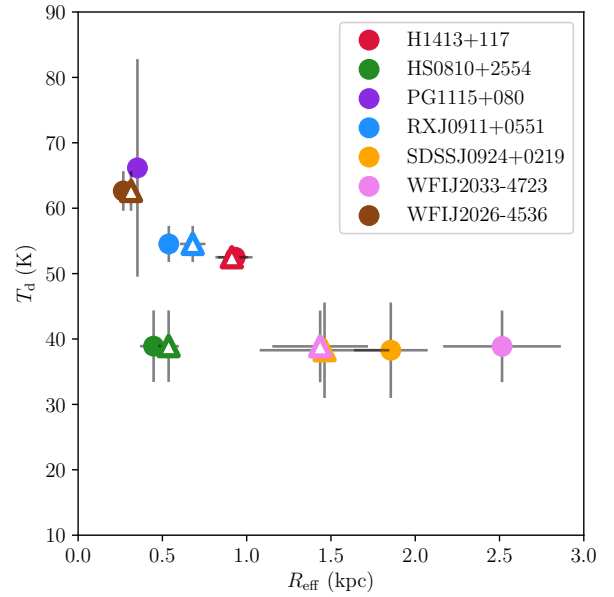

Figure 18. The effective radius (R_{eff}) of the dust continuum (solid circles) and CO line emission (open triangles) against effective dust temperature (T_{d}) for the seven lensed quasar hosts investigated here.

Fig. 18), suggesting that the dust is uniformly heated to higher temperatures by an obscured starburst, as opposed to the central AGN. This does not exclude the possibility that the AGN contributes to the cold dust emission, but in such a scenario it cannot be a significant fraction without a conspiracy between the effective radius, temperature and luminosity. The higher dust temperatures found for some quasar hosts relative to DSFGs can be explained by the more compact physical size of their dust emission.

We estimate that four compact quasar hosts in our sample have high star formation rate surface densities which may be Eddington-limited. This finding is consistent with previous investigations of H1413+117, which have independently verified an Eddington-limited starburst with radiative transfer modelling of spectral line ratios (Bradford et al. 2009; Riechers et al. 2011a; Uzgil et al. 2016). In general, while an X-ray radiation field may penetrate large column densities of molecular gas, it will not efficiently heat dust grains over large distances (Meijerink et al. 2007). These factors further suggest that the AGN are unlikely to be responsible for a significant fraction of the sub-mm dust emission. We cannot determine the origin of the molecular gas heating from single CO lines, but a comparison between multiple transitions will help constrain the contribution from the AGN to the emission reported here. Radiative transfer models of quasar hosts find that these are very likely to be enhanced by X-rays from the AGN (Vallini et al. 2019), so could probe the effect of radiative feedback on the host galaxy ISM.

Another potential source of uncertainty in the analysis by Stacey et al. (2018) was the assumption on the unknown lensing magnification of the FIR emission, which was set to be 10^{+10}_{-5} where the FIR magnification is unknown. If the lensing magnifications were significantly higher than was conservatively assumed, then the level of the inferred star formation would be much lower. From our analysis of the seven lensed quasars investigated here, we find dust magnifications factors in the range 11–24, roughly consistent with the assumption by Stacey et al. (2018). While on the higher side
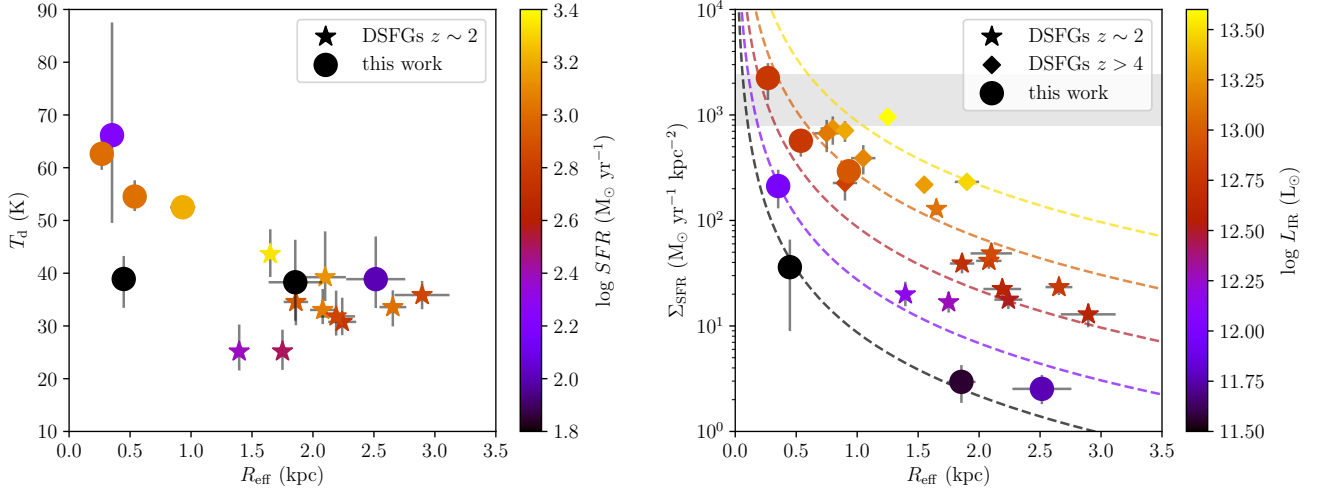
Figure 19. Left: Effective radius (R_{eff}) against effective dust temperature (T_{d}), coloured by star formation rate. Right: Effective radius against mean star formation rate surface density (Σ_{SFR}), where the grey region shows our estimated Eddington limit and its uncertainty. Σ_{SFR} and the dashed curves show the tracks for log L_{IR} values of 11.5, 12, 12.5, 13, 13.5. Circles show the quasar hosts in this work (with H1413+117 corrected for SED blending); stars show coeval DSFGs at $z \sim 2$ (Hodge et al. 2016, 2019); triangles show DSFGs at $z > 4$ (Hodge et al. 2015, 2016; Riechers et al. 2013, 2014, 2017). Four of the seven quasar hosts have star formation rate surface densities close to the Eddington limit, similar to DSFGs selected at $z > 4$.
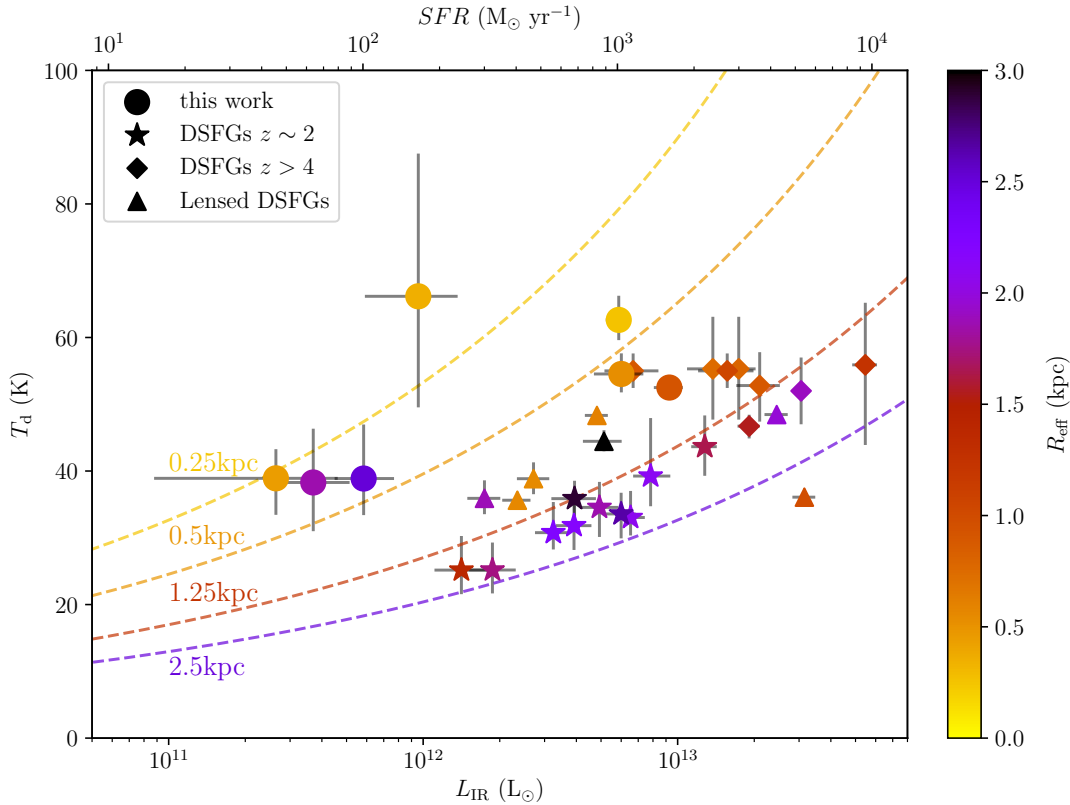
Figure 20. Effective dust temperature against infrared luminosity, coloured by effective radius. The dashed lines show the modified Stefan-Boltzmann relation from Yan & Ma (2016) for sources of indicated physical sizes, assuming a dust model with $\beta = 1.5$ and $\nu_0 = 3$ THz. Sources from this work are shown with circles. DSFGs at $z \sim 2$ are shown with stars; DSFGs at $z > 4$ are shown with diamonds; lensed DSFGs are shown with triangles. The quasar hosts in this sample have higher effective dust temperature and are generally more compact than dusty star-forming galaxies of similar infrared luminosity.

of the estimate, these are four-image lens systems so high magnifications are typical. Accounting for the inferred magnifications, we find that the star formation rates for the sample here range from 45 to 1600 $M_\odot$ yr^{-1}.

5.2 Evidence for compact quasar hosts

The quasar hosts in our study can be divided into two types: DSFGs characterised by clumpy dust distributions, with sizes and star formation rate densities similar to typical sub-mm-selected DSFGs (i.e. WFI J2033−4723 and SDSS J0924+0219), and DSFGs characterised by compact ($R_{\rm eff} < 1$ kpc) sizes and generally high star formation densities (see Fig. 19) with no evidence of clumpy features on kpc-scales[4].

The sizes of the compact quasar hosts in this work are similar to the sub-mm sizes of compact star-forming galaxies (Ikarashi et al. 2015; Barro et al. 2016, 2017). The lensed DSFGs (which we expect to represent more compact DSFGs due to their selection bias, e.g. Serjeant 2012) show a large range of sizes, yet the quasar hosts of similar luminosity are generally more compact and have higher dust temperatures. This may indicate that quasars are preferentially hosted in more compact systems. Even considering that two of these quasar hosts are likely to be selected on the basis of their FIR properties, the remaining optically selected systems are distinct from the remaining sample.

In this work, by selecting hosts of Type 1 quasars, we have explicitly chosen galaxies whose AGN are rapidly accreting and generating relativistic winds that have exposed their accretion discs. It is predicted that a significant fraction of DSFGs host AGN (e.g. Hickox et al. 2014). While it has been found that at least one in five DSFGs have an X-ray luminous AGN (Wang et al. 2013), this is true for at least half of compact star-forming galaxies (Barro et al. 2014; Kocevski et al. 2017)[5]. The relative prevalence of X-ray luminous AGN may point towards elevated black hole growth in compact DSFGs. The small size of compact galaxies requires that there has been a rapid infall of gas such that the bulk of the star formation occurs within the central region of the galaxy: this could allow the AGN to accrete more efficiently from the dense ISM.

The sub-mm sizes of both the compact DSFGs and quasar hosts are similar to the optical/infrared sizes of compact quiescent galaxies at similar redshifts ($\bar{R}_{\rm eff} = 0.9$ kpc; van Dokkum et al. 2008). Assuming the sub-mm dust emission traces the bulk of the stellar component, this is consistent with the hypothesis that compact starbursts are progenitors of compact quiescent galaxies (and ultimately massive ellipticals). The still-high star formation rates and molecular gas densities of these hosts could mean that we catch them at the moment of compaction, at the onset of gas depletion and quenching. This would require that at least some compact quiescent galaxies form rapidly, rather than through a slow evolution (Wellons et al. 2015).

Overall, the sizes of < 1 to 3 kpc we find for our sample are similar to those of Silverman et al. (2019), who found the optical/infrared sizes of quasar hosts at $z \sim 1.5$ are in the range < 1 to 6 kpc ($\bar{R}_{\rm eff} = 2.2$ kpc), intermediate between main sequence and quiescent galaxies. Additionally, Ikarashi et al. (2017) also found

that $z \sim 1$–3 quasar-starburst composites have smaller sub-mm dust sizes than both starburst-dominated DSFGs and quasars whose SEDs have a more dominant AGN fraction in the MIR. D'Amato et al. (2020) also found similar sizes for the dust components of X-ray-selected quasars at $2 < z < 5$. These results and ours are inconsistent with models that predict the size of quasar hosts to be larger than those of normal star-forming galaxies, due to adiabatic expansion that results from negative AGN feedback (Fan et al. 2008) or positive AGN feedback on kpc-scales (Ishibashi et al. 2013).

5.3 Mechanism of formation

In the context of the ongoing debate about how compact quiescent galaxies form their very high stellar densities, our finding that the host galaxies of quasars are compact is in agreement with a model whereby they form rapidly in a period of dissipative contraction. Simulations suggest that star-forming galaxies are able to maintain high star formation rates in quasi-stable discs, fed by smooth accretion from the cosmic web (e.g. Kereš et al. 2005). For a galaxy to compactify, dynamical instabilities must be induced by mergers or intense inflows that can drive gas into the centre of the galaxy on timescales shorter than the star formation rate (Zolotov et al. 2015). The high star formation rates and the existence of clumpy, non-axisymmetric dust features that we detect strongly suggest that quasar hosts are globally unstable due to gravitational fragmentation, as has been frequently observed for DSFGs (Iono et al. 2016; Oteo et al. 2017; Hodge et al. 2019).

Optical imaging of DSFGs has often found that their molecular gas and obscured star formation is significantly more compact than pre-existing stellar distributions (Simpson et al. 2015; Ikarashi et al. 2015; Kaasinen et al. 2020). The optical/UV-luminous stellar emission observed for PG 1115+080 (see Peng et al. 2006) must also be more extended or offset from the dust, as it is lensed into an Einstein ring, whereas the dust is not. These unobscured stellar features may exist for the other quasar systems we observe here, but are too faint to be seen in optical imaging or cannot be distinguished from the bright quasar emission. This UV-luminous emission likely contributes only a small fraction of the star formation, which is largely obscured, but these features may hint at the formation histories of the galaxies. For example, the unobscured stellar emission may be quenched as a result of gas compaction and stellar feedback (Maiolino et al. 2015). However, this may be difficult to interpret due to the much higher sensitivity to star formation achieved by optical/UV imaging compared to sub-mm imaging.

5.4 Mechanism of quenching

Simulations find that compaction can naturally lead to quenching, through rapid gas consumption and stellar feedback, coupled with increasing dynamical stability (Zolotov et al. 2015). Observations of dense starbursts suggest that radiation pressure from stars could be a feasible mechanism to suppress further star formation (Murray et al. 2005; Andrews & Thompson 2011). If all the dust emission we observe here is associated with star formation, the four most compact sources in our work are in the regime of Eddington-limited maximum starbursts. This is consistent with observations of compact quiescent galaxies, whose star formation histories suggest a short starburst of ~ 50 Myr before quiescence (Valentino et al. 2020). In the absence of reliable stellar mass estimates, we cannot determine whether star formation in the compact quasar hosts has begun to quench by direct comparison with DSFGs. However,

---

[4] For HS 0810+2554 there may be extended dust emission that is undetected due to the low surface brightness sensitivity of the data.

[5] We assume these are lower limits as observations are limited by sensitivity, and simulations suggest that he actual AGN contribution to the SED may be much higher (Roebuck et al. 2016).

the higher implied star formation rate surface densities imply that stellar feedback could play the primary role.

For the one system where we can trace the extent of the gas reservoir, we find a very low gas fraction in comparison to its dynamical mass. This suggests that this galaxy may be transitioning into quiescence following the depletion and removal of gas, as observed for compact star-forming galaxies at $z \sim 2$ (Spilker et al. 2016, 2019). The implied depletion timescale of 50 ± 40 Myr is comparable to the finding of ~ 100 Myr for compact star-forming galaxies by Spilker et al. (2016) and consistent with ~ 50 Myr found by Valentino et al. (2020).

The compact starbursts and implied short depletion timescales could suggest that AGN feedback is not necessary to quench or regulate star formation, contrary to simulations. However, long-term maintenance of quenching requires that the supply of fresh cold gas into the galaxy is halted. As the quasars in this work are likely hosted in massive haloes (Kormendy & Ho 2013), virial shock-heating alone could help suppress accretion of cold gas from the cosmic web (Dekel & Birnboim 2006). It is likely that AGN feedback becomes important at some point to prevent re-accretion of ejected gas (Croton et al. 2006), as the energy input from star formation falls far short of the level required to completely unbound the gas from the galaxy and maintain a quenched state. Indeed, we expect that compact galaxies quench abruptly (Valentino et al. 2020) and that 'maintenance mode' (or 'jet mode') AGN feedback tends to be observed after galaxies have already begun to quench (Hardcastle et al. 2007).

Observations of CO (1–0) in high-redshift lensed AGN-starbursts have revealed disturbed morphologies, suggestive of feedback (AGN or stellar) or ongoing major mergers (Thomson et al. 2012; Spingola et al. 2020), whilst others do not appear to show such features (Riechers et al. 2011b; Sharon et al. 2016). Such observations for this sample will be useful to understand to what extent the CO lines investigated here probe the mass and kinematics of the gas reservoir, particularly in comparison to the population of DSFGs that do not appear to host rapidly accreting AGN.

5.5 Selection effects and confusion

A source of caution in the interpretation of our findings is the combination of systematic biases that stem from the comparison of samples with different selection effects. Ideally, we would like to compare coeval samples of DSFGs and quasar hosts. However, the detection of DSFGs is strongly influenced by selection effects, such that systems with lower dust temperatures are preferentially detected at lower redshifts due to the shape of the modified black body spectrum. The selection of strongly lensed DSFGs at FIR wavelengths is much less dependent on dust temperature and expected to be more strongly dependent on source size (Serjeant 2012; Hezaveh et al. 2012). Together, these represent a diverse selection of DSFGs. The quasar systems, on the other hand, were optically selected, based on the emission from their unobscured accretion discs, and their selection was in most cases based on their lens configuration (RX J0911+0551 and H1413+117 being exceptions). Therefore, we do not implicitly select quasar hosts that have high temperatures or are more compact. However, analyses with larger samples, including less strongly magnified systems, will provide a better statistical comparison between coeval galaxy populations selected with different methods.

Notably, we identify a nearby source of one object (H1413+117) that likely causes photometric confusion at shorter wavelengths. This has the important implication that source blend-

ing may contribute to the extreme infrared luminosities found for some quasar-starbursts. Observations with ALMA of (unlensed) optically selected quasars have revealed that 30 percent of FIR identifications can be resolved into secondary counterparts that contribute at least 25 percent to the measured infrared luminosity (Hatziminaoglou et al. 2018). This may be unsurprising as massive galaxies seem to be formed in over-dense regions (Zeballos et al. 2018). The sources investigated here are gravitationally lensed, so the relative contribution from companions is expected to be lower on average than for field sources. Nevertheless, our findings suggest care should be taken to account for field sources when compiling an SED with photometric measurements obtained with low spatial resolution (e.g. *Herschel*/SPIRE).

6 CONCLUSIONS

The properties of cold dust and molecular gas in quasar hosts at cosmologically important redshifts can give insights into the mechanism responsible for the transformation of these galaxies from gas-rich, dusty starbursts into passive, quiescent systems. We have presented high angular resolution imaging with ALMA of the host galaxies of seven optically selected quasars at redshifts between 1.5 and 3. Using pixellated lens modelling, we reconstructed the sources and their intrinsic properties.

In comparison to unlensed DSFGs with similar redshifts and infrared luminosities (i.e. ALESS DSFGs and FIR-selected lensed DSFGs) and DSFGs at higher redshifts with similar dust temperatures, the quasar hosts in this work are generally more compact. The observed luminosities are broadly consistent with the expectations for more compact star formation, disputing the case for a significant contribution from black hole accretion to the global dust emission at sub-mm wavelengths.

We find that two of the quasar hosts are characterised by extended, clumpy dust distributions, but the remainder are compact starbursts. These differences may represent quasar hosts at different stages of morphological change into compact galaxies. The more compact systems have sizes that are already similar to quiescent galaxies at $z \sim 2$, with extreme star formation rate densities that imply a rapid consumption of gas. This is consistent with a picture in which the inflow of gas resulting from mergers and/or dynamical instabilities triggers both the intense starburst and a period of efficient black hole accretion (Kocevski et al. 2017). These intense starbursts could be responsible for both the formation of the high stellar densities and rapid quenching of compact galaxies.

If quasar hosts are in the process of forming stellar bulges, we should find that these systems are globally characterised by unstable gas discs and rapidly depleting gas reservoirs (Zolotov et al. 2015; Tacchella et al. 2016). Matched, high angular resolution observations of low J-level CO emission would probe the size of the cold gas reservoir and determine whether the star formation rate efficiency and gas depletion timescales of quasar hosts are significantly different relative to those of DSFGs. Furthermore, cold gas diagnostics will be useful to determine whether outflows are prevalent and whether AGN or stellar feedback is ongoing, as expected from simulations and semi-analytic models (e.g. Hopkins et al. 2008).

Our conclusions here are based on the data for just seven objects from the sample of lensed quasars. In the current observing cycle of ALMA, we will obtain data for at least 27 lensed quasars in Band 6 and 7 which will further probe the size and structure of the heated dust emission from this class of objects, and probe the

structure and kinematics of the molecular gas that is feeding both the star formation and AGN activity.

REFERENCES

ALMA Partnership et al., 2015, ApJ, 808, L4
Alloin D., Guilloteau S., Barvainis R., Antonucci R., Tacconi L., 1997, A&A, 321, 24
Andrews B. H., Thompson T. A., 2011, ApJ, 727, 97
Apostolovski Y., et al., 2019, A&A, 628, A23
Auger M. W., Treu T., Bolton A. S., Gavazzi R., Koopmans L. V. E., Marshall P. J., Moustakas L. A., Burles S., 2010, The Astrophysical Journal, 724, 511
Badole S., Jackson N., Hartley P., Sluse D., Stacey H., Vives-Arias H., 2020, MNRAS, 496, 138
Barcos-Muñoz L., et al., 2017, ApJ, 843, 117
Barro G., et al., 2013, ApJ, 765, 104
Barro G., et al., 2014, ApJ, 791, 52
Barro G., et al., 2016, ApJ, 827, L32
Barro G., et al., 2017, ApJ, 851, L40
Barvainis R., Ivison R., 2002, ApJ, 571, 712
Blain A. W., Smail I., Ivison R. J., Kneib J. P., Frayer D. T., 2002, Phys. Rep., 369, 111
Bradford C. M., et al., 2009, ApJ, 705, 112
Burud I., et al., 1998, The Messenger, 92, 29
Bussmann R. S., et al., 2013, ApJ, 779, 25
Bussmann R. S., et al., 2015, ApJ, 812, 43
Cañameras R., et al., 2017, A&A, 604, A117
Carollo C. M., et al., 2013, ApJ, 773, 112
Casey C. M., Narayanan D., Cooray A., 2014, Phys. Rep., 541, 45
Casey C. M., et al., 2018, in Murphy E., ed., Astronomical Society of the Pacific Conference Series Vol. 517, Science with a Next Generation Very Large Array. p. 629 (arXiv:1810.08258)
Chapin E. L., et al., 2011, MNRAS, 411, 505
Chen G. C. F., et al., 2019, MNRAS, 490, 1743
Cortzen I., et al., 2020, A&A, 634, L14
Croton D. J., et al., 2006, MNRAS, 365, 11
D'Amato Q., et al., 2020, A&A, 636, A37
Dale D. A., Helou G., Contursi A., Silbermann N. A., Kolhatkar S., 2001, ApJ, 549, 215

Damjanov I., et al., 2011, ApJ, 739, L44
Dekel A., Birnboim Y., 2006, MNRAS, 368, 2
Dekel A., et al., 2009, Nature, 457, 451
Di Matteo T., Springel V., Hernquist L., 2005, Nature, 433, 604
Diamond-Stanic A. M., Moustakas J., Tremonti C. A., Coil A. L., Hickox R. C., Robaina A. R., Rudnick G. H., Sell P. H., 2012, ApJ, 755, L26
Draine B. T., 2006, ApJ, 636, 1114
Dunne L., Eales S., Edmunds M., Ivison R., Alexander P., Clements D. L., 2000, MNRAS, 315, 115
Dye S., et al., 2018, MNRAS, 476, 4383
Eigenbrod A., Courbin F., Dye S., Meylan G., Sluse D., Vuissoz C., Magain P., 2006, A&A, 451, 747
Fabian A. C., 2012, ARA&A, 50, 455
Falgarone E., et al., 2017, Nature, 548, 430
Fan L., Lapi A., De Zotti G., Danese L., 2008, ApJ, 689, L101
Ferkinhoff C., Brisbin D., Nikola T., Stacey G. J., Sheth K., Hailey-Dunsheath S., Falgarone E., 2015, ApJ, 806, 260
Feroz F., Hobson M. P., Cameron E., Pettitt A. N., 2013, arXiv e-prints, p. arXiv:1306.2144
Foreman-Mackey D., Hogg D. W., Lang D., Goodman J., 2013, PASP, 125, 306
Gabor J. M., Bournaud F., 2014, MNRAS, 441, 1615
Greve T. R., et al., 2014, ApJ, 794, 142
Hardcastle M. J., Evans D. A., Croston J. H., 2007, MNRAS, 376, 1849
Harris K., et al., 2016, MNRAS, 457, 4179
Harrison C. M., 2017, Nature Astronomy, 1, 0165
Harrison C. M., et al., 2012, ApJ, 760, L15
Hartley P., Jackson N., Sluse D., Stacey H. R., Vives-Arias H., 2019, MNRAS, 485, 3009
Hatziminaoglou E., Farrah D., Humphreys E., Manrique A., Pérez-Fournon I., Pitchford L. K., Salvador-Solé E., Wang L., 2018, MNRAS, 480, 4974
Helou G., Khan I. R., Malek L., Boehmer L., 1988, ApJS, 68, 151
Hewett P. C., Wild V., 2010, MNRAS, 405, 2302
Hezaveh Y. D., Marrone D. P., Holder G. P., 2012, ApJ, 761, 20
Hezaveh Y., Dalal N., Holder G., Kuhlen M., Marrone D., Murray N., Vieira J., 2013, ApJ, 767, 9
Hezaveh Y. D., et al., 2016, ApJ, 823, 37
Hickox R. C., Mullaney J. R., Alexander D. M., Chen C.-T. J., Civano F. M., Goulding A. D., Hainline K. N., 2014, ApJ, 782, 9
Hodge J. A., da Cunha E., 2020, arXiv e-prints, p. arXiv:2004.00934
Hodge J. A., Riechers D., Decarli R., Walter F., Carilli C. L., Daddi E., Dannerbauer H., 2015, ApJ, 798, L18
Hodge J. A., et al., 2016, ApJ, 833, 103
Hodge J. A., et al., 2019, The Astrophysical Journal, 876, 130
Högbom J. A., 1974, A&AS, 15, 417
Hopkins P. F., Hernquist L., Cox T. J., Kereš D., 2008, ApJS, 175, 356
Hunter J. D., 2007, Computing in Science & Engineering, 9, 90
Ikarashi S., et al., 2015, ApJ, 810, 133
Ikarashi S., et al., 2017, ApJ, 849, L36
Inada N., et al., 2003, AJ, 126, 666
Iono D., et al., 2016, ApJ, 829, L10
Ishibashi W., Fabian A. C., Canning R. E. A., 2013, MNRAS, 431, 2350
Jackson N., Tagore A. S., Roberts C., Sluse D., Stacey H., Vives-Arias H., Wucknitz O., Volino F., 2015, MNRAS, 454, 287
Jones E., Oliphant T., Peterson P., et al., 2001, SciPy: Open source scientific tools for Python, http://www.scipy.org/
Juvela M., Ysard N., 2012, A&A, 541, A33
Kaasinen M., et al., 2020, ApJ, 899, 37
Kendall M. G., 1945, Biometrika, 33, 239
Kennicutt Jr. R. C., 1998, ApJ, 498, 541
Kereš D., Katz N., Weinberg D. H., Davé R., 2005, MNRAS, 363, 2
Kirkpatrick A., et al., 2012, ApJ, 759, 139
Kirkpatrick A., Sharon C., Keller E., Pope A., 2019, ApJ, 879, 41
Kneib J.-P., Cohen J. G., Hjorth J., 2000, ApJ, 544, L35
Kocevski D. D., et al., 2017, ApJ, 846, 112
Kormann R., Schneider P., Bartelmann M., 1994, A&A, 284, 285
Kormendy J., Ho L. C., 2013, ARA&A, 51, 511

Lelli F., Fraternali F., Sancisi R., 2010, A&A, 516, A11

Magain P., Surdej J., Swings J. P., Borgeest U., Kayser R., 1988, Nature, 334, 325

Magorrian J., et al., 1998, AJ, 115, 2285

Maiolino R., et al., 2015, MNRAS, 452, 54

Mauch T., Murphy T., Buttery H. J., Curran J., Hunstead R. W., Piestrzynski B., Robertson J. G., Sadler E. M., 2003, MNRAS, 342, 1117

McMullin J. P., Waters B., Schiebel D., Young W., Golap K., 2007, in Shaw R. A., Hill F., Bell D. J., eds, Astronomical Society of the Pacific Conference Series Vol. 376, Astronomical Data Analysis Software and Systems XVI. p. 127

Meijerink R., Spaans M., Israel F. P., 2007, A&A, 461, 793

Mihos J. C., Hernquist L., 1996, ApJ, 464, 641

Morgan N. D., Caldwell J. A. R., Schechter P. L., Dressler A., Egami E., Rix H.-W., 2004, AJ, 127, 2617

Mosquera A. M., Kochanek C. S., 2011, ApJ, 738, 96

Murray N., Quataert E., Thompson T. A., 2005, ApJ, 618, 569

Naab T., Johansson P. H., Ostriker J. P., Efstathiou G., 2007, ApJ, 658, 710

Naab T., Johansson P. H., Ostriker J. P., 2009, ApJ, 699, L178

Nayyeri H., et al., 2016, ApJ, 823, 17

Negrello M., et al., 2017, MNRAS, 465, 3558

Oteo I., et al., 2016, ApJ, 827, 34

Oteo I., Zwaan M. A., Ivison R. J., Smail I., Biggs A. D., 2017, ApJ, 837, 182

Page M. J., et al., 2012, Nature, 485, 213

Peng C. Y., Impey C. D., Rix H.-W., Kochanek C. S., Keeton C. R., Falco E. E., Lehár J., McLeod B. A., 2006, ApJ, 649, 616

Pitchford L. K., et al., 2016, MNRAS, 462, 4067

Planck Collaboration et al., 2016, A&A, 594, A13

Powell D., Vegetti S., McKean J. P., Spingola C., 2020, arXiv e-prints, p. arXiv:2005.03609

Reimers D., Hagen H. J., Baade R., Lopez S., Tytler D., 2002, A&A, 382, L26

Riechers D. A., Walter F., Carilli C. L., Cox P., Weiss A., Bertoldi F., Menten K. M., 2011a, ApJ, 726, 50

Riechers D. A., et al., 2011b, ApJ, 739, L32

Riechers D. A., et al., 2013, Nature, 496, 329

Riechers D. A., et al., 2014, ApJ, 796, 84

Riechers D. A., et al., 2017, ApJ, 850, 1

Rizzo F., Vegetti S., Fraternali F., Di Teodoro E., 2018, MNRAS, 481, 5606

Rizzo F., Vegetti S., Powell D., Fraternali F., McKean J. P., Stacey H. R., White S. D. M., 2020, Nature, 584, 201

Roebuck E., Sajina A., Hayward C. C., Pope A., Kirkpatrick A., Hernquist L., Yan L., 2016, ApJ, 833, 60

Rosario D. J., et al., 2013, ApJ, 763, 59

Rusu C. E., et al., 2020, MNRAS,

Rybak M., McKean J. P., Vegetti S., Andreani P., White S. D. M., 2015a, MNRAS, 451, L40

Rybak M., Vegetti S., McKean J. P., Andreani P., White S. D. M., 2015b, MNRAS, 453, L26

Schaye J., et al., 2015, MNRAS, 446, 521

Schulze A., et al., 2019, MNRAS, 488, 1180

Scoville N., et al., 2014, ApJ, 783, 84

Serjeant S., 2012, MNRAS, 424, 2429

Sérsic J. L., 1963, Boletin de la Asociacion Argentina de Astronomia La Plata Argentina, 6, 41

Sharon C. E., Riechers D. A., Hodge J., Carilli C. L., Walter F., Weiß A., Knudsen K. K., Wagg J., 2016, ApJ, 827, 18

Sijacki D., Springel V., Di Matteo T., Hernquist L., 2007, MNRAS, 380, 877

Silverman J. D., et al., 2019, ApJ, 887, L5

Simpson J. M., et al., 2015, ApJ, 799, 81

Sluse D., Chantry V., Magain P., Courbin F., Meylan G., 2012, A&A, 538, A99

Solomon P. M., Vanden Bout P. A., 2005, ARA&A, 43, 677

Somerville R. S., Davé R., 2015, ARA&A, 53, 51

Somerville R. S., Hopkins P. F., Cox T. J., Robertson B. E., Hernquist L., 2008, MNRAS, 391, 481

Spilker J. S., et al., 2016, ApJ, 826, 112

Spilker J. S., et al., 2018, Science, 361, 1016

Spilker J. S., Bezanson R., Weiner B. J., Whitaker K. E., Williams C. C., 2019, ApJ, 883, 81

Spingola C., et al., 2020, MNRAS, 495, 2387

Stacey H. R., et al., 2018, MNRAS, 476, 5075

Stanley F., et al., 2017, MNRAS, 472, 2221

Swinbank A. M., et al., 2010, Nature, 464, 733

Swinbank A. M., et al., 2014, MNRAS, 438, 1267

Tacchella S., Dekel A., Carollo C. M., Ceverino D., DeGraf C., Lapiner S., Mand elker N., Primack J. R., 2016, MNRAS, 458, 242

The Astropy Collaboration et al., 2018, preprint, (arXiv:1801.02634)

Thomson A. P., et al., 2012, MNRAS, 425, 2203

Trujillo I., et al., 2006, ApJ, 650, 18

Tuan-Anh P., Hoai D. T., Nhung P. T., Diep P. N., Phuong N. T., Thao N. T., Darriulat P., 2017, MNRAS, 467, 3513

Uzgil B. D., Bradford C. M., Hailey-Dunsheath S., Maloney P. R., Aguirre J. E., 2016, ApJ, 832, 209

Valentino F., et al., 2020, ApJ, 889, 93

Vallini L., Tielens A. G. G. M., Pallottini A., Gallerani S., Gruppioni C., Carniani S., Pozzi F., Talia M., 2019, MNRAS, p. 2427

Vegetti S., Koopmans L. V. E., 2009, MNRAS, 392, 945

Wales D., Doye J., 1998, The Journal of Physical Chemistry A, 101

Wang S. X., et al., 2013, ApJ, 778, 179

Weiß A., Downes D., Neri R., Walter F., Henkel C., Wilner D. J., Wagg J., Wiklind T., 2007, A&A, 467, 955

Wellons S., et al., 2015, MNRAS, 449, 361

Wellons S., Faucher-Giguère C.-A., Anglés-Alcázar D., Hayward C. C., Feldmann R., Hopkins P. F., Kereš D., 2020, MNRAS,

Weymann R. J., Latham D., Angel J. R. P., Green R. F., Liebert J. W., Turnshek D. A., Turnshek D. E., Tyson J. A., 1980, Nature, 285, 641

Williams C. C., et al., 2014, ApJ, 780, 1

Yan H., Ma Z., 2016, The Astrophysical Journal, 820, L16

Zeballos M., et al., 2018, MNRAS, 479, 4577

Zhang Z.-Y., Romano D., Ivison R. J., Papadopoulos P. P., Matteucci F., 2018, Nature, 558, 260

Zolotov A., et al., 2015, MNRAS, 450, 2327

van Dokkum P. G., et al., 2008, ApJ, 677, L5

van Dokkum P. G., et al., 2015, ApJ, 813, 23

Table 3. Parameters of the lens models for the seven lensed quasars. We give the median and percentile ranges of the likelihood-weighted posterior probability distribution found with MultiNest, where the maximum a posteriori model parameters are given in square brackets. For WFI 2033−4723, parameters for the secondary lenses are also given. Parameters denoted by '≡' are fixed as detailed in Section 3. The power-law index, ζ, is 2.16 for PG 1115+080 (Chen et al. 2019), 1.95 for WFI 2033−4723 (Rusu et al. 2020) and 2.0 for all other lenses. δx and δy positions are relative to the phase centre positions given in Table 1; κ_0 is the normalised convergence; e is the ellipticity of lens; γ is the reduced external shear. In all cases, position angles are measured East of North.

	δx (")	δy (")	κ_0 (")	e	θ_e (°)	γ	θ_γ (°)
HS 0810+2554	0.277 ± 0.008 [0.278]	0.839 ± 0.013 [0.841]	0.470 ± 0.005 [0.470]	0.26 ± 0.03 [0.28]	32.6 ± 2.7 [29.9]	0.005 ± 0.003 [0.009]	98 ± 50 [112]
RX J0911+0551	-0.972 ± 0.031 [−0.965]	2.422 ± 0.015 [2.424]	1.099 ± 0.021 [1.099]	0.25 ± 0.08 [0.27]	-66 ± 10 [−67]	0.350 ± 0.024 [0.382]	9.7 ± 1.4 [10.3]
SDSS J0924+0219	0.257 ± 0.011 [0.255]	0.037 ± 0.008 [0.044]	0.888 ± 0.008 [0.892]	0.36 ± 0.05 [0.39]	-96.1 ± 3.6 [−95.5]	0.020 ± 0.015 [0.022]	-4 ± 41 [2]
PG 1115+080	1.700 ± 0.013 [1.701]	0.967 ± 0.010 [0.965]	1.036 ± 0.013 [1.030]	$\equiv 0.892$	$\equiv 96.9$	0.153 ± 0.007 [0.149]	58.5 ± 0.8 [58.3]
H1413+117	0.131 ± 0.007 [0.135]	0.331 ± 0.010 [0.333]	0.640 ± 0.070 [0.640]	0.45 ± 0.05 [0.46]	16 ± 5 [16]	0.051 ± 0.013 [0.054]	51 ± 13 [54]
WFI J2026−4536	$\equiv 0.0125$	$\equiv 0.385$	0.667 ± 0.019 [0.668]	0.275 ± 0.012 [0.278]	-73.7 ± 1.9 [−73.8]	0.090 ± 0.004 [0.090]	-109 ± 1 [−109]
WFI J2033−4723	-0.799 ± 0.015 [−0.801]	-1.298 ± 0.018 [−0.129]	0.967 ± 0.016 [0.977]	0.12 ± 0.06 [0.12]	25.7 ± 9.2 [29.5]	0.20 ± 0.02 [0.19]	12.7 ± 1.9 [12.4]
	$\equiv 3.301$	$\equiv -1.243$	$\equiv 0.93$	$\equiv 0.33$	$\equiv 38.5$	-	-
	$\equiv -0.868$	$\equiv 0.817$	$\equiv 0.001$	-	-	-	-

Table 4. The properties of the reconstructed continuum emission, corrected for lensing magnification. For H1413+117 we give values after correcting the SED for photometric confusion (see Section 2.6). Note that for all except WFI J2033−4723 and PG 1115+080, the quoted sizes include an additional ±10% uncertainty due to empirical scatter in the slope of the mass profile (see Section 4.1 for details).

	μ_{dust}	R_{dust} (kpc)	n	T_d^{cold} (K)	T_d^{warm} (K)	β	L_{FIR} (L⊙)	SFR (M⊙ yr⁻¹)	Σ_{SFR} (M⊙ yr⁻¹ kpc⁻²)	M_d (M⊙)
HS 0810+2554	24 ± 4	0.46 ± 0.10	0.57 ± 0.05	39^{+4}_{-5}	135^{+25}_{-18}	$\equiv 2$	$8^{+5}_{-5} \times 10^{11}$	45^{+35}_{-30}	40^{+30}_{-30}	$1.2^{+0.4}_{-0.5} \times 10^7$
RX J0911+0551	10.6 ± 0.2	0.54 ± 0.06	0.56 ± 0.04	54^{+3}_{-3}	–	$1.9^{+0.1}_{-0.1}$	$1.8^{+0.2}_{-0.2} \times 10^{12}$	600^{+80}_{-70}	300^{+70}_{-70}	$6.7^{+1.7}_{-1.7} \times 10^6$
SDSS J0924+0219	15.1 ± 0.7	1.9 ± 0.2	1.2 ± 0.1	38^{+8}_{-7}	–	$1.5^{+0.6}_{-0.4}$	$2.7^{+0.9}_{-0.7} \times 10^{11}$	90^{+30}_{-20}	5^{+2}_{-2}	$5.3^{+1.0}_{-0.8} \times 10^7$
PG 1115+080	14.6 ± 0.4	0.35 ± 0.04	0.47 ± 0.01	66^{+17}_{-21}	–	$1.9^{+0.3}_{-0.3}$	$3.6^{+1.6}_{-1.3} \times 10^{11}$	120^{+50}_{-40}	310^{+150}_{-125}	$3.7^{+2.3}_{-1.5} \times 10^6$
H1413+117	11.2 ± 0.2	0.9 ± 0.1	0.66 ± 0.07	53^{+1}_{-1}	246^{+14}_{-24}	$1.88^{+0.04}_{-0.04}$	$4.9^{+0.6}_{-0.6} \times 10^{12}$	1600^{+200}_{-200}	290^{+80}_{-80}	$1.2^{+0.1}_{-0.1} \times 10^8$
WFI J2026−4536	19.6 ± 0.8	0.31 ± 0.03	0.61 ± 0.02	63^{+4}_{-3}	–	$1.8^{+0.1}_{-0.1}$	$3.1^{+1.7}_{-1.5} \times 10^{12}$	1010^{+60}_{-50}	2200^{+900}_{-900}	$3.9^{+0.1}_{-0.1} \times 10^7$
WFI J2033−4723	17.6 ± 0.9	2.5 ± 0.2	1.1 ± 0.2	31^{+7}_{-5}	–	$1.7^{+0.3}_{-0.3}$	$4.6^{+1.3}_{-1.0} \times 10^{11}$	150^{+40}_{-30}	3^{+1}_{-1}	$4.5^{+0.8}_{-0.7} \times 10^7$

Table 5. The properties of the reconstructed CO line emission, corrected for lensing magnification. For SDSS J0924+0219 and WFI J2033−4723, the Sérsic index, n, is fixed to a value of 1 (consistent with the value found for the dust continuum). All parameters are derived from moment maps of the reconstructed source. Note that for all except WFI J2033−4723 and PG 1115+080, the quoted sizes include an additional ±10% uncertainty due to empirical scatter in the slope of the mass profile (see Section 4.1 for details).

|	$\bar{\mu}_{CO}$	R_{CO} (kpc)	n	I_{CO} (Jy km s⁻¹)	L_{CO} (L⊙)	L'_{CO} (K km s⁻¹ pc²)	M_{dyn} (M⊙)
HS 0810+2554	20.3 ± 0.7	0.52 ± 0.03	0.57 ± 0.03	0.19 ± 0.01	$(3.4 \pm 0.1) \times 10^6$	$(2.6 \pm 0.1) \times 10^9$	$(3.5 \pm 2.1) \times 10^{10}$
RX J0911+0551	10.3 ± 0.2	0.7 ± 0.1	0.56 ± 0.01	0.47 ± 0.01	$(4.2 \pm 0.1) \times 10^7$	$(6.9 \pm 0.1) \times 10^9$	$(1.2 \pm 0.6) \times 10^{10}$
SDSS J0924+0219	17 ± 1	1.5 ± 0.4	$\equiv 1.0$	0.13 ± 0.01	$(6.4 \pm 0.4) \times 10^6$	$(2.5 \pm 0.2) \times 10^8$	$(1.0 \pm 0.5) \times 10^{10}$
H1413+117	11.1 ± 0.2	0.9 ± 0.1	0.54 ± 0.05	3.4 ± 0.1	$(4.8 \pm 0.1) \times 10^8$	$(1.34 \pm 0.02) \times 10^{10}$	$(2.4 \pm 0.4) \times 10^{10}$
WFI J2026−4536	19.6 ± 0.8	0.31 ± 0.03	0.52 ± 0.03	0.54 ± 0.02	$(6.6 \pm 0.3) \times 10^7$	$(1.4 \pm 0.1) \times 10^9$	$(4.0 \pm 0.3) \times 10^9$
WFI J2033−4723	17 ± 2	1.4 ± 0.3	$\equiv 1.0$	0.026 ± 0.003	$(1.5 \pm 0.2) \times 10^6$	$(6.1 \pm 0.7) \times 10^7$	$(2.1 \pm 1.2) \times 10^9$

SUPPLEMENTARY FIGURES AND TABLES

Table 1. List of DSFGs used in this study and their properties. (†) notes where the dust temperature is obtained from the literature (from an optically thick dust model); in all other cases, the SED fitting was performed in this work using the methodology described in Section 4.2. For the unlensed DSFGs, the sizes are taken from the literature; for the lensed DSFGs, the sizes and ALMA photometry are derived with the same methodology used for the lensed quasar systems in this work.

|	z	T_d (K)	L_{FIR} (10^{12} L$_\odot$)	R_{eff} (kpc)	Ref
$z \sim 2$ DSFGs					
ALESS 3.1	3.374	43^{+5}_{-4}	$6.7^{+0.8}_{-0.8}$	1.6 ± 0.1	[1,2]
ALESS 5.1	2.86	33^{+4}_{-3}	$3.4^{+0.5}_{-0.4}$	2.1 ± 0.1	[3,2]
ALESS 10.1	2.02	36^{+3}_{-3}	$2.1^{+0.4}_{-0.4}$	2.9 ± 0.4	[3,2]
ALESS 15.1	2.67	34^{+3}_{-4}	$3.1^{+0.4}_{-0.4}$	2.7 ± 0.2	[1,2]
ALESS 17.1	1.540	25^{+4}_{-4}	$1.0^{+0.2}_{-0.2}$	1.8 ± 0.1	[1,2]
ALESS 29.1	1.439	25^{+5}_{-4}	$0.7^{+0.2}_{-0.2}$	1.4 ± 0.1	[3,2]
ALESS 39.1	2.44	31^{+5}_{-3}	$1.7^{+0.3}_{-0.3}$	2.2 ± 0.1	[3,2]
ALESS 45.1	2.34	32^{+5}_{-4}	$2.1^{+0.4}_{-0.3}$	2.2 ± 0.2	[3,2]
ALESS 67.1	2.123	39^{+9}_{-5}	$4.1^{+0.8}_{-0.6}$	2.1 ± 0.2	[3,2]
ALESS 112.1	2.315	35^{+4}_{-4}	$2.6^{+0.5}_{-0.4}$	1.9 ± 0.1	[1,2]
$z > 4$ DSFGs					
ALESS 9.1	4.867	47^{+6}_{-7}	10^{+1}_{-1}	1.6 ± 0.1	[1,2]
ADFS 27 (1)	5.655	55^{+8}_{-8} †	$9.1^{+1.5}_{-1.5}$	0.8 ± 0.1	[4]
ADFS 27 (2)			$7.2^{+1.5}_{-1.5}$	0.8 ± 0.1	[4]
HFLS 3	6.334	56^{+9}_{-12} †	29^{+3}_{-3}	1.3 ± 0.1	[5]
AzTEC 3	5.299	53^{+5}_{-5} †	11^{+2}_{-2}	0.9 ± 0.1	[6]
GN20	4.055	52^{+5}_{-5} †	16^{+1}_{-1}	1.9 ± 0.1	[7]
SGP 196076(1)	4.425	55^{+3}_{-3} †	8^{+2}_{-2}	1.1 ± 0.1	[8]
SGP 196076(2)			4^{+1}_{-1}	0.9 ± 0.1	[8]
Lensed DSFGs					
HELMS 5	3.503	48^{+1}_{-1}	$2.5^{+0.3}_{-0.3}$	0.54 ± 0.01	[9,10]
HELMS 8	1.195	36^{+1}_{-1}	$1.2^{+0.2}_{-0.2}$	0.52 ± 0.02	[10,11]
HELMS 9	1.441	36^{+3}_{-2}	$0.9^{+0.1}_{-0.1}$	1.6 ± 0.3	[10,11]
HELMS 13	2.765	44^{+2}_{-1}	$2.7^{+0.5}_{-0.5}$	3.8 ± 1.1	[10,11]
HELMS 22	2.509	36^{+1}_{-1}	$16.5^{+1.7}_{-1.7}$	0.94 ± 0.02	[10,11]
G15v2.779	4.243	48^{+1}_{-1}	$12.8^{+1.3}_{-1.3}$	1.72 ± 0.2	[10,11]
G15v2.19	1.027	39^{+2}_{-2}	$1.4^{+0.3}_{-0.2}$	0.43 ± 0.02	[10,11]

References: [1] Hodge et al. (2019); [2] Swinbank et al. (2010); [3] Hodge et al. (2016); [4] Riechers et al. (2017); [5] Riechers et al. (2013); [6] Riechers et al. (2014); [7] Cortzen et al. (2020); [8] Oteo et al. (2016); [9] Nayyeri et al. (2016); [10] Stacey et al. in prep; [11] Dye et al. (2018)
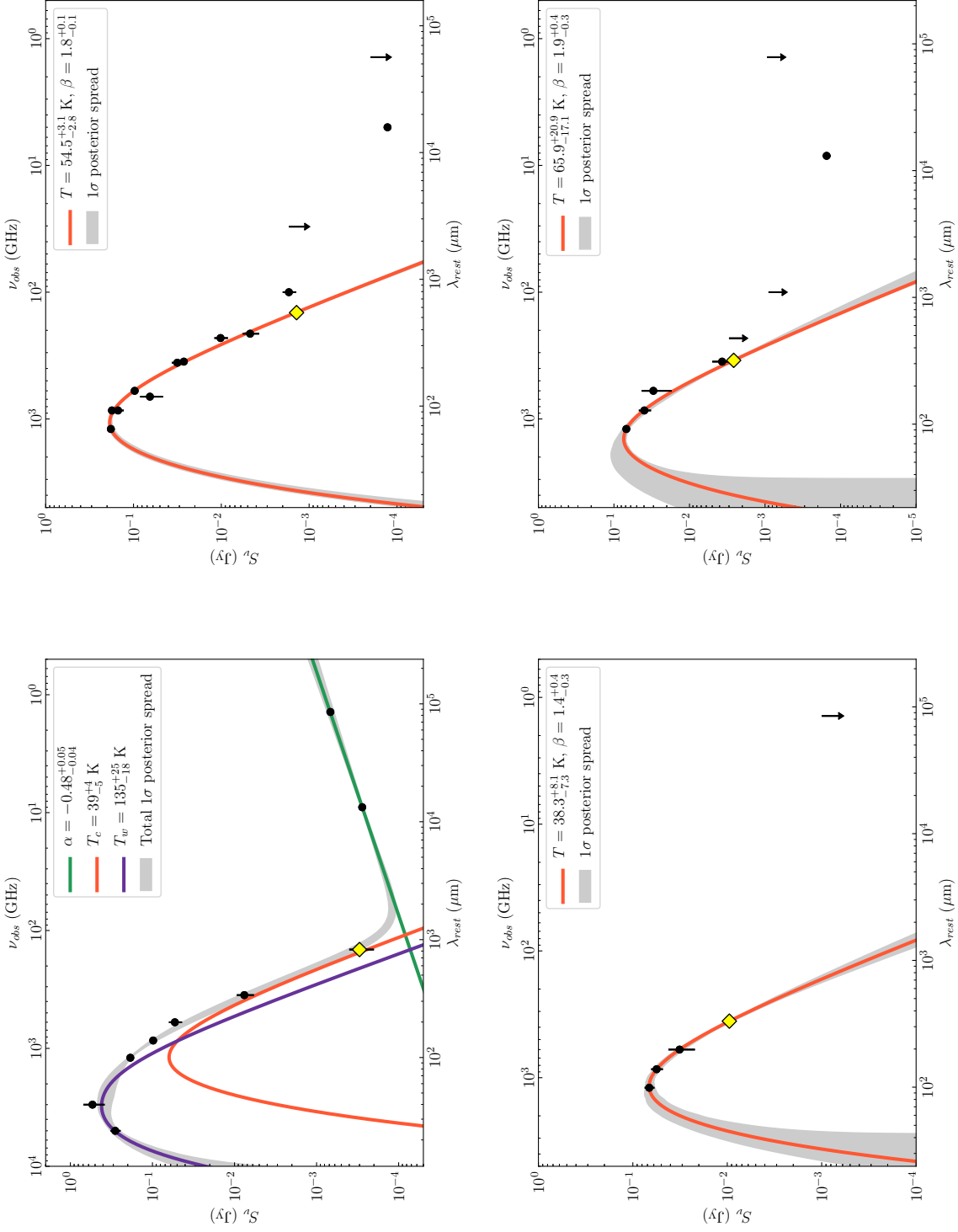
Figure 1. SED fits from FIR to radio wavelengths. Top row, HS 0810+2554 and RX J0911+0551; bottom row, SDSS J0925+0219 and PG 1115+080. The data are fit with one or two modified black body component for thermal dust emission (orange and purple), and for HS 0810+2554 a power-law for radio synchrotron emission (green). The grey shaded region shows the 1σ distribution of the posterior from the MCMC sampling. The flux density measurement from this work is shown by a yellow diamond; ancillary data points are listed and referenced in Stacey et al. (2018).
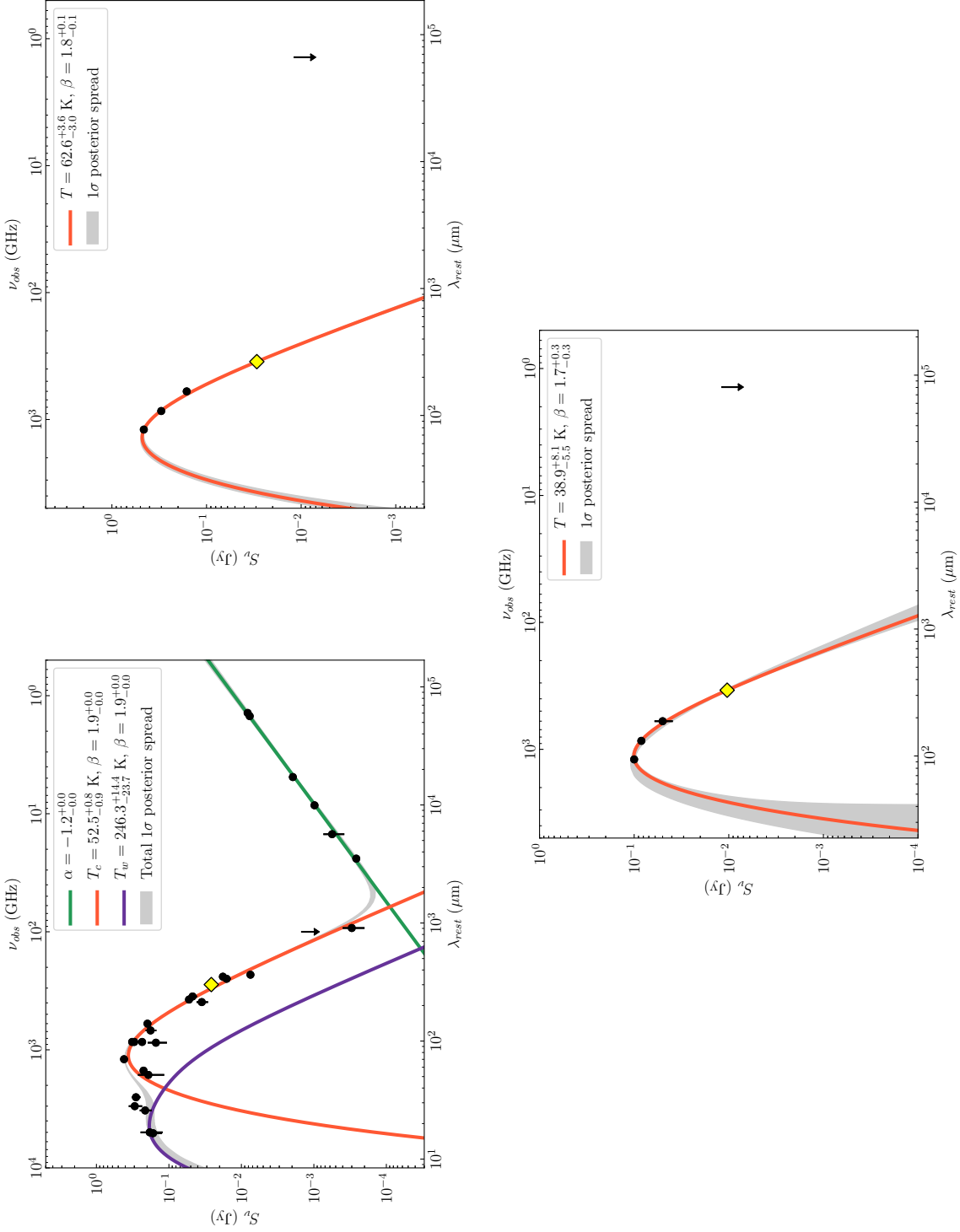
Figure 2. SED fits from FIR to radio wavelengths for the sample. Top row, H1413+117 and WFI J2033−4723; bottom, WFI J2026−4536. For H1413+117, data above 300 GHz has been scaled by a factor of 0.8 to account for blending. The data are fit with one or two modified black body component for thermal dust emission (orange and purple), and for H1413+117, a power-law for radio synchrotron emission (green). The grey shaded region shows the 1σ distribution of the posterior from the MCMC sampling. The flux density measurement from this work is shown by a yellow diamond; ancillary data points are listed and referenced in Stacey et al. (2018).
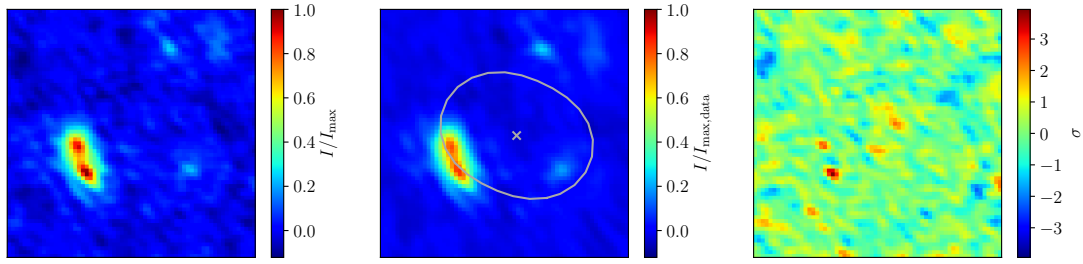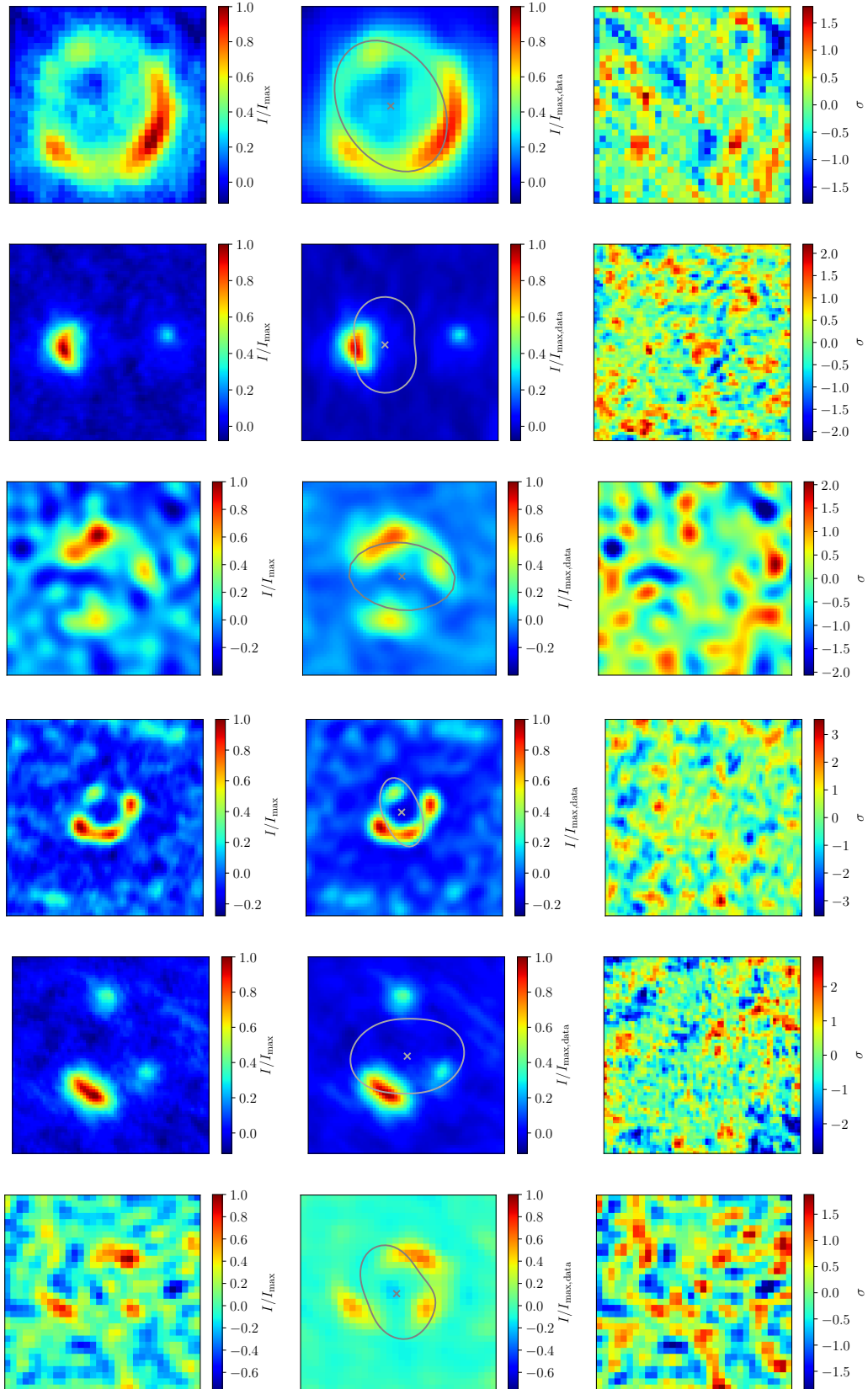
Figure 3. Grid-based lens models of the continuum data for PG 1115+080. Panels, left to right, show the dirty image of the data in arbitrary flux units, the dirty image of the model on the same scale as the data, and the residuals (data−model) in units of σ, where σ is the rms noise of the visibilities. The lens position and critical curve is shown in grey.

This paper has been typeset from a TEX/LATEX file prepared by the author.
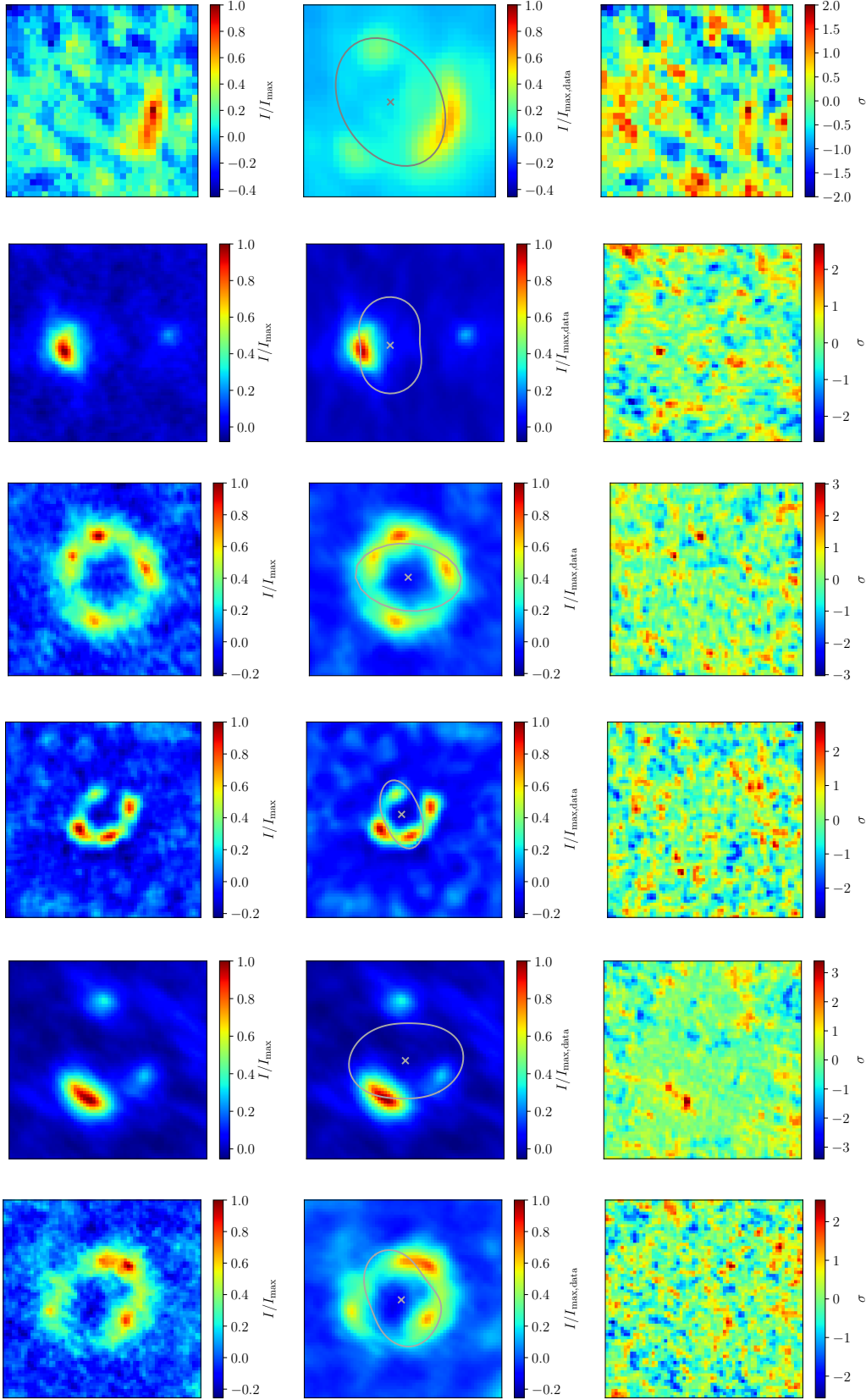
Figure 4. Grid-based lens models of the continuum data. The rows, top to bottom, show HS 0810+2554, RX J0911+0551, SDSS 0924+0219, WFI 2026−4536 and WFI 2033−4723. Panels, left to right, show the dirty image of the data in arbitrary flux units, the dirty image of the model on the same scale as the data, and the residuals (data−model) in units of σ, where σ is the rms noise of the visibilities. The lens position and critical curve is shown in grey.

Figure 5. Grid-based lens modelling of the integrated CO line data. Rows, top to bottom, show HS 0810+2554, RX J0911+0551, SDSS 0924+0219, H1413+117, WFI 2026−4536 and WFI 2033−4723. Panels, left to right, show the dirty image of the data in arbitrary flux units, the dirty image of the model (on the same scale as the data), and the residuals (data−model) in units of σ, where σ is the rms noise of the visibilities. The lens position and critical curve is shown in grey.